PHYSICAL REVIEW FLUIDS **6**, 063403 (2021)

Thermal effects mediating the flow induced by laser-induced optical breakdown

Jonathan M. Wang,[1,*] Marco Panesi,[2,†] and Jonathan B. Freund[2,‡]
[1]Department of Mechanical Science and Engineering, University of Illinois at Urbana-Champaign, Urbana, Illinois 61801, USA
[2]Department of Aerospace Engineering, University of Illinois at Urbana-Champaign, Urbana, Illinois 61801, USA

(Received 3 January 2021; accepted 8 June 2021; published 30 June 2021)

A short focused laser pulse can generate a hot plasma, which expands then contracts and can eject a hot jet, the speed and direction of which is sensitive to the details of the plasma kernel. The coupling of thermal and chemical nonequilibrium plasma mechanisms with this hydrodynamic development is assessed with detailed simulations of a two-temperature, three-species plasma model. Time scales for electron recombination, thermal relaxation, and diffusion are compared to that of the plasma expansion to anticipate conditions in which these mechanisms might affect the vorticity generation that leads to the ultimate flow pattern. The effect of these mechanisms are analyzed through comparison with corresponding inert-gas and equilibrium models. Thermal-nonequilibrium effects are found to be weak due to rapid relaxation of the heavy-particle and electronic temperatures. In contrast, chemical equilibration occurs at a rate comparable to the expansion and thereby enhance both it and subsequent hydrodynamic mechanisms as the energy stored in ion formation during the preceding breakdown is released by electron recombination. Thermal conduction, enhanced by high-temperature free electrons, weakens the ejection.

DOI: 10.1103/PhysRevFluids.6.063403

I. INTRODUCTION

Optical breakdown of a gas [1] by a ∼10–100 mJ focused laser generates an elongated millimeter-scale, high-temperature plasma kernel that in turn generates a complex vortical flow region [2,3]. The heating causes a rapid expansion, followed by asymmetric contraction and sometimes ejections of hot gas, which can travel many times the length of the initial plasma kernel [3]. The specific flow characteristics can depend qualitatively on gas conditions: for example, for otherwise identical conditions, ejections towards the laser source for $p = 1$ atm [4,5] reverse for higher pressures [6]. This late-time ($t \gtrsim 100\,\mu$s) ejecting flow pattern results primarily from hydrodynamic processes and that are sensitive to the geometry of the plasma kernel, which in turn induce differences in the vorticity generated during the $t \lesssim 10\,\mu$s plasma expansion [7–9]. In a combustible mixture, the resulting distribution of relaxing hot plasma remnants, rich in radical species, can subsequently affect ignition and flame growth in a combustible mixture [10–12]. Figure 1 illustrates an evolution leading to a hydrodynamic ejection.

This flow sensitivity warrants an assessment of how the hydrodynamic development couples with chemical- and thermal-nonequilibrium mechanisms of the plasma, which was neglected in the

---

[*] Corresponding author: jmwang14@stanford.edu
[†] mpanesi@illinois.edu
[‡] jbfreund@illinois.edu

©2021 American Physical Society

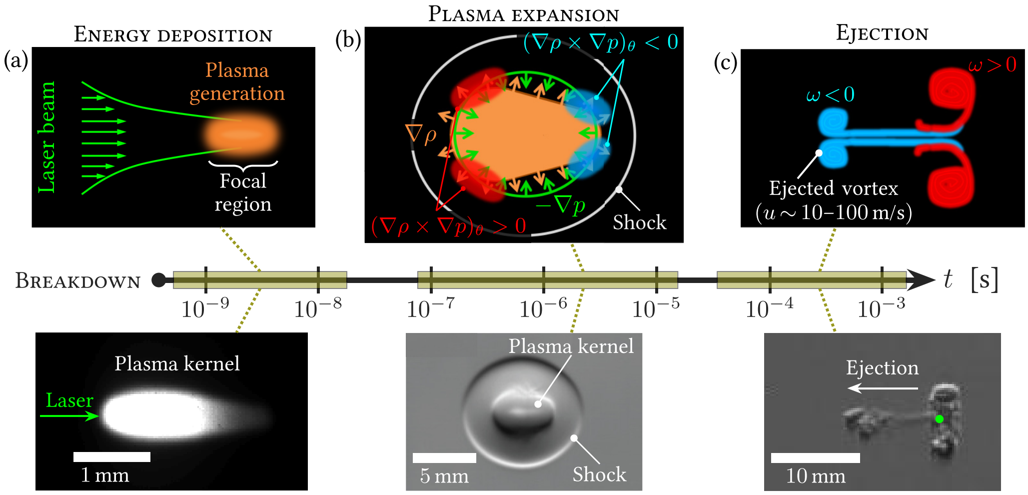

FIG. 1. Schematic of a typical post-breakdown evolution. (a) The focused laser generates a plasma kernel that (b) expands and generates vorticity ω by baroclinic torque $(\nabla\rho\times\nabla p)/\rho^2$ (azimuthal component shown) resulting from misaligned density gradients $\nabla\rho$ (due to low kernel density) and pressure gradients ∇p (in the postshock rarefaction). (c) This vorticity advects and forms the ejected vortex ring. These stages are also shown in images from experiments (J. E. Retter and G. S. Elliott, personal communication; see also a related study [13]); the green dot indicates the nominal laser focus.

simpler models of previous flow studies [9,14]. Nonequilibrium is understood to be significant in laser-induced plasmas and has been studied extensively [15–17], though typically for spectroscopy applications. Inert, perfect-gas models [9,18,19] reproduce the primary mechanisms of the observed ejection but preclude analysis of nonequilibrium-plasma effects. Extending these perfect-gas models to include equilibrium chemistry and appropriate transport properties for plasmas yields qualitatively similar flow [18], though details of how this affects the ejection remain unclear. Two-temperature and finite-rate chemistry nonequilibrium models are available [20,21] and have been applied to blunt-body drag reduction using laser-induced plasma, but were not used for detailed study of the breakdown-generated flow. Highly detailed models, with up to three temperatures and 19 species for air, have been used to describe the laser-plasma coupling and the early $t\lesssim 10$ ns breakdown [22–24], though they are computationally expensive and have not been extended to the longer times ($t\gtrsim 10\,\mu$s) of the eventual gas-dynamic ejection.

The goal here is to explicitly include plasma-transport and thermal- and chemical-nonequilibrium mechanisms in order to isolate their influence on post-breakdown hydrodynamics, particularly the ultimate ejection of hot gases from the plasma kernel. It will be confirmed that these models reproduce observed phenomena, which is an important validation, but we focus on the flow mechanisms rather than maximizing fidelity of the plasma representation that would be needed to precisely describe early times [22]. An axisymmetric simulation model of a two-temperature, singly ionized plasma with three-species finite-rate chemistry is introduced in Sec. II. It is parameterized to represent argon. To isolate plasma effects, results are compared to a corresponding two-species, inert-gas model, also introduced in Sec. II. To anticipate when the nonequilibrium plasma might influence the ejection, in Sec. III we quantify timescales of heavy-species and electron diffusion, electron recombination, and thermal relaxation in spherical simulations for ambient pressures from 0.1 atm to 10 atm. These suggest conditions for timescale overlap with the plasma expansion, during which the vorticity that mediates the subsequent hydrodynamic development is generated. Electron recombination, which occurs at a rate comparable to or faster than this expansion, is studied in Sec. IV. In Sec. V detailed comparison with the inert-gas model for $p_\infty = 0.5$ atm shows how high thermal conductivity, enhanced by free electrons, can weaken the ejection. Conclusions are summarized in Sec. VI.

II. SIMULATION METHODOLOGY AND MODELS

A. Nonequilibrium plasma model

1. Physical model

For simplicity, the plasma is taken to be singly ionized and monatomic with neutral species A and its ion A^+. These share a single heavy-particle temperature T_h, and the out-of-equilibrium electron temperature is T_e. The flow is governed by

$$\frac{\partial \rho}{\partial t} + \nabla \cdot \rho \boldsymbol{u} = 0, \tag{1}$$

$$\frac{\partial \rho \boldsymbol{u}}{\partial t} + \nabla \cdot \rho \boldsymbol{u}\boldsymbol{u} + \nabla \cdot (p\boldsymbol{I} - \boldsymbol{\tau}) = \boldsymbol{0}, \tag{2}$$

$$\frac{\partial \rho(e + |\boldsymbol{u}|^2/2)}{\partial t} + \nabla \cdot [\rho(e + |\boldsymbol{u}|^2/2)\boldsymbol{u}] + \nabla \cdot [(p\boldsymbol{I} - \boldsymbol{\tau})\boldsymbol{u}] + \nabla \cdot \boldsymbol{q} = 0, \tag{3}$$

$$\frac{\partial \rho e_e}{\partial t} + \nabla \cdot \rho e_e \boldsymbol{u} + \nabla \cdot p_e \boldsymbol{u} + \nabla \cdot \boldsymbol{q}_e = \boldsymbol{u} \cdot \nabla p_e + \frac{3}{2} n_e k_b (T_h - T_e)\left(\frac{1}{\tau_{eA^+}} + \frac{1}{\tau_{eA}}\right) - I_A \dot{n}_{e,1}, \tag{4}$$

$$\frac{\partial \rho Y_{A^+}}{\partial t} + \nabla \cdot \rho Y_{A^+} \boldsymbol{u} + \nabla \cdot \rho Y_{A^+} \boldsymbol{V}_{A^+} = m_{A^+} \dot{n}_{A^+}, \tag{5}$$

with ideal-gas state relation

$$p = \rho k_b \left(\frac{Y_e}{m_e} T_e + \frac{Y_{A^+}}{m_{A^+}} T_h + \frac{Y_A}{m_A} T_h\right), \tag{6}$$

where k_b is the Boltzmann constant, e is the internal energy, p is the pressure, ρ is the mass density, $\boldsymbol{u}$ is the velocity, n_k is the species-k number density, Y_k is its mass fraction, m_k is its atomic mass, and $\dot{n}_k$ is its production rate [25–27]. The electronic energy e_e (A1) is computed with a single excited level for both A and A^+. The electron pressure is $p_e = \rho Y_e k_b T_e / m_e$, and I_A is the ionization potential of A. For specificity, argon properties are used throughout for m_A, I_A, and all other gas properties. Charge separation effects are not expected to be significant, particularly after the laser pulse when there is no external electric field. Even for plasma kernel initially at 30 000 K in ambient pressure 0.1 atm, the Debye length is 0.1 μm, which is much smaller than the grid resolution and the length scales relevant to the present analysis, and so local charge neutrality ($n_e = n_{A^+}$) is assumed.

The viscous stress tensor in (2) and heat flux vectors in (3) and (4) are

$$\boldsymbol{\tau} = \mu(\nabla \boldsymbol{u} + \nabla \boldsymbol{u}^T) + \left(\mathcal{B} - \frac{2}{3}\mu\right)(\nabla \cdot \boldsymbol{u})\boldsymbol{I}, \tag{7}$$

$$\boldsymbol{q} = -\lambda_h \nabla T_h - \lambda_{el} \nabla T_e + \rho \sum_k Y_k h_k \boldsymbol{V}_k, \tag{8}$$

$$\boldsymbol{q}_e = -\lambda_{el} \nabla T_e + \rho \sum_k Y_k h_{e,k} \boldsymbol{V}_k, \tag{9}$$

where μ is the dynamic viscosity, λ_h and λ_{el} are the heavy-particle and free-electron thermal conductivities, and h_k and $h_{e,k}$ are the total and electronic enthalpies. Bulk viscosity $\mathcal{B}$ in (7) is zero for an ideal monatomic gas [28], though we use (and validate) an artificial-viscosity model for shocks [29,30]; details are given in Sec. II D. The diffusion velocity $\boldsymbol{V}_k$ is modeled assuming an ambipolar mechanism [31,32]. All transport properties are computed with standard models and mixture rules [33–35]. The thermal relaxation times τ_{eA^+} and τ_{eA} in (4) are modeled with established cross sections that have been used to model hypersonic boundary layers and shocks in argon [33,36].

The specifics of these plasma model components are intricate but standard and are provided in Appendix A.

The kinetics model includes two ionization-recombination processes:

$$A + e^- \rightleftharpoons A^+ + e^- + e^-, \tag{10}$$

$$A + A \rightleftharpoons A^+ + e^- + A, \tag{11}$$

which respectively have rates of progress

$$\mathcal{R}_1 = k_{f,1}(T_e)\left(n_e n_A - \frac{1}{K_{\text{eq}}(T_e)} n_e^2 n_{A^+}\right), \tag{12}$$

$$\mathcal{R}_2 = k_{f,2}(T_h)\left(n_A^2 - \frac{1}{K_{\text{eq}}(T_h)} n_A n_e n_{A^+}\right), \tag{13}$$

where the rate constants $k_{f,1}$ and $k_{f,2}$ are based on those developed by Hoffert and Lien [37], and $K_{\text{eq}}(T)$ is the Saha equilibrium constant [38]. The production rates in (4) and (5) are $\dot{n}_{A^+} = \dot{n}_e = -\dot{n}_A = \mathcal{R}_1 + \mathcal{R}_2$; $\dot{n}_{e,1}$ in (4) corresponds to the free-electron production by electron-impact ionization in (10) [37]. Resonant charge-exchange reactions such as $A + A^+ \rightleftharpoons A^+ + A$, while typically having a large cross section, are not included in the chemistry model as they would not alter $\dot{n}_k$ in (4) and (5), though their effect on transport coefficients is included (Appendix A).

Although this relatively simple plasma description is selected to facilitate our analysis, it is also quantitatively accurate. For example, it reproduces key features of a Mach 15.9 shock in argon, including its relaxation length and unsteady character (Appendix B). This confirms that it provides a reasonable model for key timescales in such a plasma. Radiation can be an important factor in some plasma regimes but is shown in Appendix C to be insignificant for the present results.

B. Two-species model

The plasma model is compared to a corresponding two-species, inert-gas model. One species (labeled I) represents the ionized gas, and the other species (labeled A) represents the neutral gas. Of course, it is not possible to match all the properties of the plasma with an inert-gas model, so some choices are made to make comparisons conclusive. In particular, choosing the atomic weight of I to be half that of A allows it to match both the peak temperature T_0/T_∞ and pressure p_0/p_∞ of the nonequilibrium model. Without this, there is little hope for any quantitative comparison; for example, a single-species model with deposited energy adjusted to match T_0/T_∞ would have a peak pressure only half that of the nonequilibrium model, which in turn would directly alter the hydrodynamics. As will be shown in Secs. IV and V, this choice to match the temperature and pressure, rather than total energy, facilitates analysis of the pressure-driven expansion and vorticity generation.

For this model the flow is governed by (1)–(3) in addition to a transport equation, expressed here for the neutral species as

$$\frac{\partial \rho Y_A}{\partial t} + \nabla \cdot \rho Y_A \boldsymbol{u} + \nabla \cdot \rho Y_A \boldsymbol{V}_A = 0, \tag{14}$$

and the equation of state is

$$p = \rho \frac{\overline{R}}{W} T, \tag{15}$$

where $W = (Y_A/W_A + Y_I/W_I)^{-1}$ is the mean molecular weight, with $W_A = 2W_I = 40$ g/mol for argon, and Y_A and $Y_I = 1 - Y_A$ are the mass fractions of the neutral and ionized gas. The specific heat $c_{p,k} = 5\overline{R}/2W_k$ is assumed constant. Both species are modeled with the same temperature-dependent

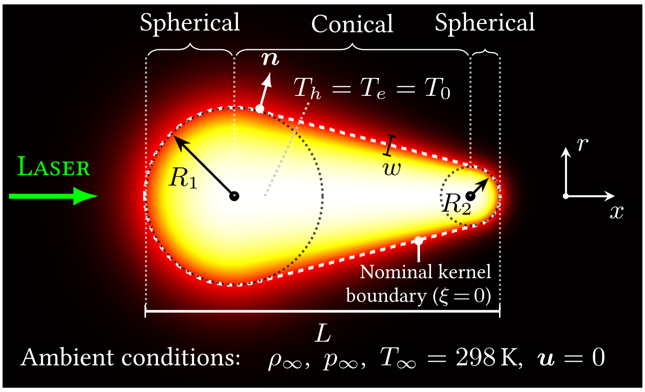

FIG. 2. Energy of the model post-breakdown plasma kernel with peak temperature T_0.

viscosity:

$$\frac{\mu}{\mu_\infty} = \left(\frac{T}{T_\infty}\right)^{0.7}. \tag{16}$$

The thermal conductivity $\lambda = c_{p,A}\mu/\mathrm{Pr}$ and diffusion coefficient $D = \lambda/\rho_\infty c_{p,A}\mathrm{Le}$ are computed assuming constant Prandtl number $\mathrm{Pr} = 0.66$ (except in Sec. V) and Lewis number $\mathrm{Le} = 1$, with $\mu_\infty = 2.24 \times 10^{-5}$ Pa s for argon. The stress tensor, heat flux, and diffusion velocity are

$$\boldsymbol{\tau} = \mu\left[(\nabla\boldsymbol{u} + \nabla\boldsymbol{u}^T) - \frac{2}{3}(\nabla\cdot\boldsymbol{u})\boldsymbol{I}\right] + \mathcal{B}(\nabla\cdot\boldsymbol{u})\boldsymbol{I}, \tag{17}$$

$$\boldsymbol{q} = \lambda\nabla T, \tag{18}$$

$$\boldsymbol{V}_k = -\frac{D}{Y_k}\nabla Y_k. \tag{19}$$

This two-species model describes a single-temperature, chemically frozen gas and facilitates comparison with similar models reported previously [9,14,18,19]. A single-temperature equilibrium-plasma model, which matches the nonequilibrium model of Sec. II A but assumes $T_e = T_h$ and an equilibrium composition, will be used to further isolate nonequilibrium effects in Sec. IV.

C. Breakdown model

Because the laser-energy deposition is much faster ($t \lesssim 10$ ns) than the dynamics of interest ($t \gtrsim 1\,\mu$s), the flow is simply initialized at $t = 0$ with the energy distribution visualized in Fig. 2. Its shape is based on images of plasma kernels after the laser pulse [3,39–42], and this particular parametrization has been shown to be able to reproduce key features of the post-breakdown hydrodynamic evolution when the geometry is varied [9,14]. The internal energy,

$$e - e_\infty = \Delta e_0 f(n), \tag{20}$$

is taken to vary only in the direction normal to the kernel boundary, where $f(n) \equiv \frac{1}{2}[1 - \tanh(\sigma n)]$ and σ is set so that $f(w/2) = 0.1$ and $f(-w/2) = 0.9$. The energy distribution blends smoothly to the $T_\infty = 298$ K ambient gas over local length scale $w \in [R_2, R_1]$, which varies tangentially in the conical section, and Δe_0 is specified based on the initial peak temperature T_0.

The overall aspect ratio α and ratio of the end radii β are

$$\alpha \equiv \frac{L}{2R_1} \quad \text{and} \quad \beta \equiv \frac{R_1}{R_2}. \tag{21}$$

Neither the prepulse density ρ_∞ nor the quiescent flow $\boldsymbol{u} = 0$ are modified. The total energy deposited is $E_0 = \int \rho_\infty (e - e_\infty)\, d^3\boldsymbol{x}$. The dynamics—particularly the timescales—of a corresponding diameter-L spherically symmetric kernel with the same volume will be analyzed in Secs. III and IV.

Although nonequilibrium mechanisms are fundamental during absorption of the laser pulse [23], the resulting plasma is thought to achieve local thermodynamic equilibrium (LTE) before its subsequent expansion, based on temperature and electron number density measurements [43]. It is also anticipated that, for the pressures of interest, collisions dominate radiative processes in establishing LTE [15,44]. Though additional conditions [17,45] may be necessary to fully achieve LTE, it is a well-defined starting point and sufficient for the present goals. The kernel is thus initialized with $T_h = T_e$, such that the internal energy e has the distribution shown in Fig. 2, and the ionization degree $\phi = n_e/(n_A + n_{A^+}) = X_e/(1 - X_e)$ satisfies

$$\frac{\phi^2}{1-\phi} = \frac{m_A}{\rho}\frac{2g^0_{A^+}}{g^0_A}\left(\frac{2\pi m_e k_b T_e}{h^2}\right)^{3/2} \exp\left(-\frac{I_A}{k_b T_e}\right), \tag{22}$$

based on the Saha equilibrium relation [28]. Similar approaches for equilibrium initialization have been employed previously [46,47].

To quantify any sensitivity to this initialization, auxiliary simulations of a spherically symmetric kernel are initialized with two alternative approaches, keeping total energy fixed: (1) in thermal nonequilibrium in which $T_{e,0} = 2T_{h,0}$, and (2) in chemical nonequilibrium with an "over-ionized" plasma for which the electron concentration is elevated to correspond to (22) at a temperature $T_{s,0} = 2T_{e,0}$ that is twice the electron temperature, where T_s is the Saha temperature (25) to be discussed in Sec. III. These initializations are based on the fact that the laser radiation interacts primarily with free electrons [22]. Even at $p_\infty = 0.1$ atm, selected to accentuate any possible sensitivity, the evolution of both cases matches that of the equilibrium initialization. As will be shown in Sec. III, thermal equilibration occurs faster than all transport or chemical processes considered, and so $T_e \approx T_h$ before any significant flow develops. Because the high-temperature kernel is almost fully ionized ($X_e \approx 0.5$) even in equilibrium, increasing the electron concentration alters the initial composition and subsequent evolution only marginally.

The baseline two-species model of Sec. II B is also initialized using (22), with the distribution of X_I determined from $X_I = 2\phi/(1+\phi) = X_e + X_{A^+}$.

D. Numerical methods

In all cases, the governing equations are discretized with an explicit fourth-order Runge-Kutta time-integration scheme and nine-point, eighth-order, centered finite-difference stencils for first and second spatial derivatives. Artificial bulk viscosity is used to model the localized shock dissipation:

$$\mathcal{B} = \overline{C\rho|D^4(\nabla\cdot\boldsymbol{u})H(-\nabla\cdot\boldsymbol{u})|}, \tag{23}$$

where $C = 7.0$ is a parameter, H is the Heaviside step function, D^4 is a mesh-dependent biharmonic-like operator, and the overbar denotes Gaussian filtering [29,30]. The shock leaves the area of interest early in the simulations, so there is no expected sensitivity of results to this approach. Third- and fourth-order derivatives are computed with sixth-order, seven-point, centered finite-difference stencils. A nine-point, eighth-order, compact filter (D3) [48] is used when the shock is strong ($t \lesssim 2\,\mu$s), after which a nine-point, eighth-order, explicit filter (D2) is used.

At the $r = 0$ coordinate singularity, the governing equations are evaluated in their $r \to 0$ limit with

$$u_r = 0, \quad \frac{\partial\rho}{\partial r} = 0, \quad \frac{\partial T_h}{\partial r} = 0, \quad \frac{\partial T_e}{\partial r} = 0, \quad \frac{\partial u_x}{\partial r} = 0, \quad \frac{\partial^2 u_r}{\partial r^2} = 0, \quad \text{and} \quad \frac{\partial Y_k}{\partial r} = 0.$$

TABLE I. Summary of meshes. For stretched meshes, the listed mesh spacing is for $\Delta x_{\text{min}} = \Delta r_{\text{min}}$.

Model	Type	Mesh spacing	Full domain	Uniform region	Mesh points
Nonequilibrium ($t < 1.1\,\mu$s)	Uniform	1.4 μm	6.05 mm × 2.38 mm	6.05 mm × 2.38 mm	4320 × 1700
Nonequilibrium	Stretched	1.6 μm	18 mm × 9 mm	8.4 mm × 4.2 mm	5760 × 2880
Two-species	Stretched	6 μm	40 mm × 20 mm	18.6 mm × 9.4 mm	3600 × 1800

All discretization stencils are modified to preserve spatial order of accuracy at $r = 0$. At the outer boundaries, outflow conditions are specified using a characteristic formulation for reacting flows [49] with $T_e = T_h$.

For the nonequilibrium model, the kernel is simulated first on a uniform mesh until the shock nearly reaches the boundary, which occurs at $t = 1.1\,\mu$s for the primary case introduced in Sec. IV. After this, the solution is interpolated using bicubic splines onto the nearly uniform region of a stretched, coarser mesh (Table I), where the mesh spacings Δx and Δr are both within 1% of their minima $\Delta x_{\text{min}} = \Delta r_{\text{min}}$; details are reported elsewhere [9]. All analyses are conducted in this nearly uniform region. In the stretched outer region, a damping term is added to the governing equations to suppress reflections [50,51]. For the two-species model, the solution is computed with a single simulation on a stretched mesh.

Electron thermal conduction $\nabla \cdot (\lambda_{el} \nabla T_e)$ typically imposed the greatest time-step restriction, with numerical stability requiring $\Delta t < 10^{-12}$ s in some cases for the mesh resolutions in Table I. Given the long timescale on which the hydrodynamic ejection forms ($t \sim 10^{-5}$ s), we apply a three-point, second-order, explicit filter to $\nabla \cdot (\lambda_{el} \nabla T_e)$ when computing the electronic heat flux $\nabla \cdot \boldsymbol{q}_e$ in (4) to narrow its represented wave-number spectrum and reduce its time-step restriction. This intentionally aggressive filter is consecutively applied four times for each evaluation of $\nabla \cdot (\lambda_{el} \nabla T_e)$. Insensitivity to this filter, which plays a role similar to what an implicit time integration would, is confirmed with spherically symmetric simulations (Appendix D).

The time step is adjusted to maintain numerical stability. For the primary $p_\infty = 0.5$ atm, $L = 2$ mm case in Sec. V, this required $\Delta t \in [10\text{ ps}, 70\text{ ps}]$. A broader range of conditions ($L \in [0.29\text{ mm}, 4.62\text{ mm}]$, $p_\infty \in [0.1\text{ atm}, 10\text{ atm}]$) is analyzed in Sec. III, for which $\Delta t \in [1\text{ ps}, 100\text{ ps}]$ is used; this is limited by chemistry for high pressures and by diffusion for low pressures and small kernels. Insensitivity to the time step is confirmed in Appendix E.

For convenience, the mole fraction of electrons in the ambient gas was set to $X_{e,\infty} = 10^{-8}$, which is high relative to equilibrium but extremely small relative to the plasma kernel values. Doing this avoids calculation of spurious electron temperatures T_e where both the electronic energy e_e and electron concentration Y_e are small (e.g., $T_e = 2m_e e_e/3k_b Y_e$ for an unexcited gas). It also relaxes the spatial resolution required to resolve the rapid decrease of free electrons at the perimeter of the kernel. Insensitivity to this choice of $X_{e,\infty}$ is demonstrated in Appendix D.

A passive scalar ξ is used to define and track the evolving kernel shape, particularly its $\xi = 0$ boundary as labeled in Fig. 2. It is initialized with the signed distance $\xi(t = 0) = n$ from the $n = 0$ boundary and subsequently advects:

$$\frac{\partial \rho \xi}{\partial t} + \nabla \cdot \rho \xi \boldsymbol{u} = 0. \tag{24}$$

III. TIMESCALES

A. Overview

To anticipate conditions in which chemical or thermal mechanisms might couple with the hydrodynamic development, plasma timescales are compared to that of the expansion. Corresponding

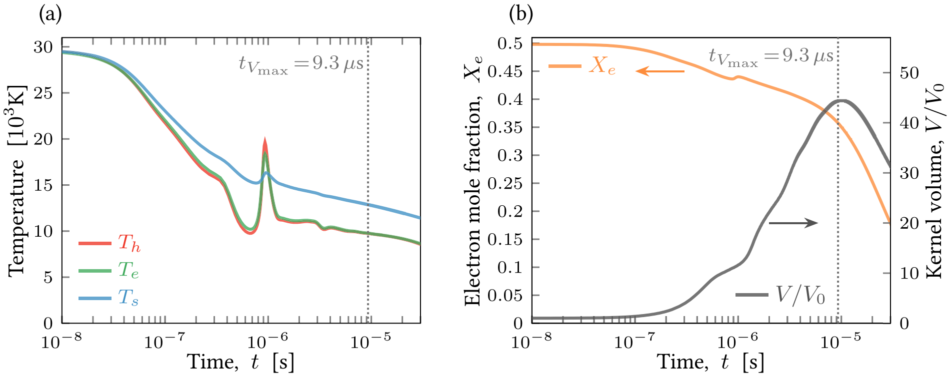

FIG. 3. Spherically symmetric case with $p_\infty = 0.1$ atm and initial diameter $L = 1.16$ mm: (a) temperatures T_h, T_e, and T_s, and (b) kernel volume V and the electron mole fraction X_e at $r = 0$. V_0 is the initial kernel volume.

perfect-gas simulations [9] suggest that this expansion phase is when the vortical structures form that will subsequently lead to the most prominent flow features.

Because the flow and plasma conditions evolve significantly in this expansion phase, it is challenging to *a priori* ascribe relevant timescales. It is expected that the plasma density and temperature decrease during the expansion, which in turn affects all collisional rates. Multiple mechanisms can be anticipated to couple. For example, as a strongly exothermic process, electron recombination alters the transport properties and, as will be shown, enhances the plasma expansion by its heat release. Thermal diffusion counteracts this heating and, if sufficiently rapid, is anticipated to weaken the expansion and accelerate cooling. The specifics of the nonlinear dynamics are expected to depend on the evolving plasma state, particularly the free-electron concentration. The rates underlying many of these mechanisms will depend on the initial gas density, and acoustic and flow speeds introduce additional timescales that depend on the initial kernel size.

Due to these complexities, and in order to analyze a range of conditions, we first consider the expansion of a spherically symmetric kernel. The timescales of the multiple mechanisms involved will guide analysis of the corresponding axisymmetric configuration and its vorticity generation (Secs. IV and V).

B. Spherical configuration

The spherically symmetric kernel is initialized with $T_0 = 30\,000$ K, as described in Sec. II C; this temperature is comparable to those observed after the laser pulse in experiments [41,52] and simulations [22,53]. The evolution for an example case with diameter $L = 1.16$ mm and $p_\infty = 0.1$ atm, corresponding to $E_0 = 11.5$ mJ energy deposited, is shown in Fig. 3. To quantify the degree of chemical nonequilibrium, we define a Saha temperature T_s [54] based on (A14) such that

$$\frac{n_e n_{A^+}}{n_A} = 2\frac{g^0_{A^+}}{g^0_A}\left(\frac{2\pi m_e k_b T_s}{h^2}\right)^{3/2} \exp\left(-\frac{I_A}{k_b T_s}\right). \tag{25}$$

This temperature provides a measure of the amount of ionization relative to $T_s = T_e$ equilibrium, with $T_s > T_e$ corresponding to n_e greater than the Saha equilibrium concentration.

The kernel is initialized with $T_h = T_e = T_s$ and peak $X_e = 0.5$ [Fig. 3(a)], after which the temperatures T_h and T_e decrease due to the expansion. The resulting $T_s > T_e$ triggers recombination, which decreases X_e [Fig. 3(b)] and counteracts the falling T_e by the electron-heating $-I_A\dot{n}_{e,1}$ term in (4), which reflects to the rate of energy gained by the free electron in (10). This recombination results in decreasing T_s according to (25). For the parameters of this particular case, recombination occurs slower than the expansion, leading to $T_s > T_e$ [Fig. 3(a)] with ionization significantly above

TABLE II. Timescales for relevant mechanisms.

Electron diffusion	$\tau_D = \dfrac{R^2\overline{W}}{\pi^2 W_A \overline{D}_{\mathrm{amb}}}$
Heavy-particle thermal conduction	$\tau_{\lambda_h} = \dfrac{R^2\overline{\rho}\,\overline{c}_p^t}{\pi^2\overline{\lambda}_h}$
Electron thermal conduction	$\tau_{\lambda_{el}} = \dfrac{R^2\overline{\rho}\,\overline{c}_p^e}{\pi^2\overline{\lambda}_{el}}$
Electron recombination	$\tau_{\mathrm{rec}} = \dfrac{\overline{n}_e}{\overline{\mathcal{R}}_{1,b} + \overline{\mathcal{R}}_{2,b}}$
Thermal relaxation	$\tau_{\mathrm{rel}} = \left(\dfrac{1}{\tau_{eA}} + \dfrac{1}{\tau_{eA^+}}\right)^{-1}$

equilibrium. Even after $t_{V_{\max}}$, thermal conduction continues to lower T_e at a rate sufficient to maintain $T_e < T_s$. In contrast, T_h and T_e do not deviate significantly due to rapid thermal relaxation; this behavior will be similar over a range of p_∞ and L (Sec. III D). The increase in T_h and T_e at $t = 9 \times 10^{-7}$ s results from rarefaction-initiated inward flow compressing gas at the origin, resembling observations of spherical blasts [55,56], though this transient will not have a significant cumulative effect for the timescale analysis in Sec. III D. This particular kernel attains its maximum volume at $t_{V_{\max}} = 9.3\,\mu$s, after which the expansion reverses and the kernel contracts [Fig. 3(b)].

C. Evolving timescales

To quantify the relative rates of various processes, we formulate timescales based on evolving volume-averaged kernel properties. Diffusion rates and both thermal and chemical relaxation rates are considered. In Sec. III D these scales will be integrated over the period of the plasma expansion to estimate their potential cumulative role for a range of initial conditions.

Mean kernel temperatures $\overline{T}_h$ and $\overline{T}_e$ are defined such that

$$\overline{\rho e}_h = \frac{3}{2}\left(\frac{\overline{\rho Y}_A}{m_A} + \frac{\overline{\rho Y}_{A^+}}{m_{A^+}}\right) k_b \overline{T}_h \tag{26}$$

and

$$\overline{\rho e}_e = \frac{3}{2}\frac{\overline{\rho Y}_e}{m_e} k_b \overline{T}_e + \sum_{k\in\{A,A^+\}} \overline{\rho Y}_k \frac{g_k^1 \exp\left(-\frac{\varepsilon_k}{k_b \overline{T}_e}\right)}{g_k^0 + g_k^1 \exp\left(-\frac{\varepsilon_k}{k_b \overline{T}_e}\right)} \frac{\varepsilon_k}{m_k}, \tag{27}$$

where

$$\overline{\rho Y}_k = \frac{1}{V}\int_{\mathcal{V}} \rho Y_k \, d^3\boldsymbol{x}, \quad \overline{\rho e}_h = \frac{1}{V}\int_{\mathcal{V}} \rho e_h \, d^3\boldsymbol{x}, \quad \text{and} \quad \overline{\rho e}_e = \frac{1}{V}\int_{\mathcal{V}} \rho e_e \, d^3\boldsymbol{x}, \tag{28}$$

for the volume-V region $\mathcal{V}$ enclosed by the $\xi = 0$ surface (24). These definitions are such that a volume-V kernel with uniform $\overline{T}_h$, $\overline{T}_e$, and $\overline{\rho Y}_k$ would have $\overline{\rho e}_h V$ heavy-particle energy, $\overline{\rho e}_e V$ electronic energy, and $\overline{\rho Y}_k V$ species-k mass. Specific timescales are summarized in Table II, where $\overline{(\,\cdot\,)}$ represents properties computed with the mean kernel properties in (26)–(28). The details of their formulation are given in Appendix F.

Figure 4 shows how each timescale in Table II evolves. Consistent with expectation, these change significantly. For example, the decreasing kernel density $\overline{\rho}$ [by a factor of $V_{\max}/V_0 = 44$; Fig. 3(b)] increases diffusion rates (τ_D, τ_{λ_h}, $\tau_{\lambda_{el}}$) but slows collisional processes (τ_{rec}, τ_{rel}), while decreasing T_h and T_e [by a factor of 3; Fig. 3(a)] alters all collisional cross sections and transport properties. These timescale variations will be averaged in order to define a representative scale for the cumulative effect of each process throughout the post-breakdown plasma expansion.

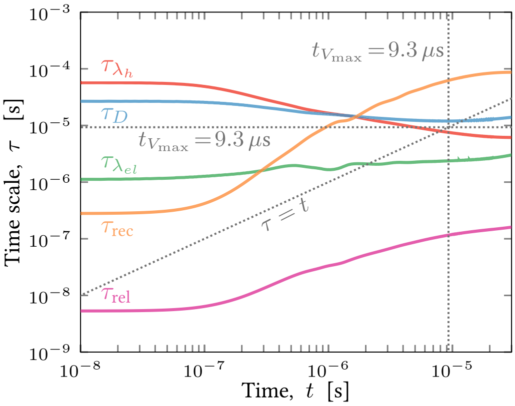

FIG. 4. Evolution of the timescales (Table II) for $L = 1.16$ mm and $p_\infty = 0.1$ atm, corresponding to the case in Fig. 3. The straight reference lines indicate possible overlap of mechanisms for this particular case with $t_{V_{\max}} = 9.3\,\mu$s.

D. Accumulated timescale estimates

To estimate net influences, we accumulate timescales τ in Table II over $t \in [0,\ t_{V_{\max}}]$ by time integration:

$$\tau^{\text{acc}} = \left[\frac{1}{t_{V_{\max}}}\int_0^{t_{V_{\max}}} \frac{1}{\tau}\,dt\right]^{-1}. \tag{29}$$

This provides an estimate of the relative importance of their corresponding processes and motivate the more detailed study in Sec. V.

The analysis focuses on kernel diameters $L \in [0.29\text{ mm},\ 4.62\text{ mm}]$ and ambient pressures $p_\infty \in [0.1\text{ atm},\ 10\text{ atm}]$ based on conditions in which laser-induced gaseous breakdown is observed. While obviously gas-dependent, $p_\infty = 0.1$ atm represents an approximate lower threshold for typical lasers [41,52,57], and kernels as small as $L \approx 0.5$ mm have been generated [3,58]. Though still lower pressures or smaller kernels would accentuate certain nonequilibrium effects, as will be discussed, viscosity and diffusion are also anticipated to suppress the flow of interest in this limit; for example, for $L = 0.5$ mm, $p_\infty = 0.1$ atm, and parameters otherwise matching the subsequent two-species axisymmetric configuration (Sec. V), the ejection fails to form.

The main concern here is the conditions under which the plasma timescales τ^{acc} overlap with the hydrodynamic expansion time $t_{V_{\max}}$. Figure 5 illustrates this. The expansion time $t_{V_{\max}}$ increases with diameter L, and for nearly all cases it is well approximated by $3L/a_\infty$, where a_∞ is the ambient speed of sound. This correspondence between $t_{V_{\max}}$ and L/a_∞ is consistent with the expected role of an acoustic timescale [9]. The time $t_{V_{\max}}$ is largely insensitive to p_∞, though for small kernels [e.g., $L = 0.29$ mm; Fig. 5(c)] rapid dissipation of energy at low p_∞ slows the expansion and leads to a modestly earlier contraction.

Thermal relaxation $\tau^{\text{acc}}_{\text{rel}}$ is the most rapid process considered, with a trend in Fig. 5 that is consistent with the expected proportionality to n_∞^{-1} based on (A11). While disparity between T_e and T_h can occur at $p_\infty = 0.1$ atm [Fig. 6(c)] due to slow collision rates, $T_e - T_h$ is relatively small ($T_e - T_h \leqslant 100$ K) for most cases. Thermal nonequilibrium effects are therefore not anticipated to directly alter the flow significantly (Sec. V), except possibly at low pressure ($p_\infty \lesssim 0.01$ atm) or for small kernels ($L \lesssim 0.1$ mm).

Free-electron thermal conduction ($\tau^{\text{acc}}_{\lambda_{el}}$) is the fastest among the diffusion timescales τ^{acc}_D, $\tau^{\text{acc}}_{\lambda_h}$, and $\tau^{\text{acc}}_{\lambda_{el}}$. Because these all increase as $\tau^{\text{acc}} \propto n_\infty = p_\infty/k_b T_\infty$ and become slower for larger L kernels, they are not directly important for higher pressures ($p = 10$ atm) or larger kernels. However, they can overlap with $t_{V_{\max}}$ for lower pressures and will be central to subsequent considerations

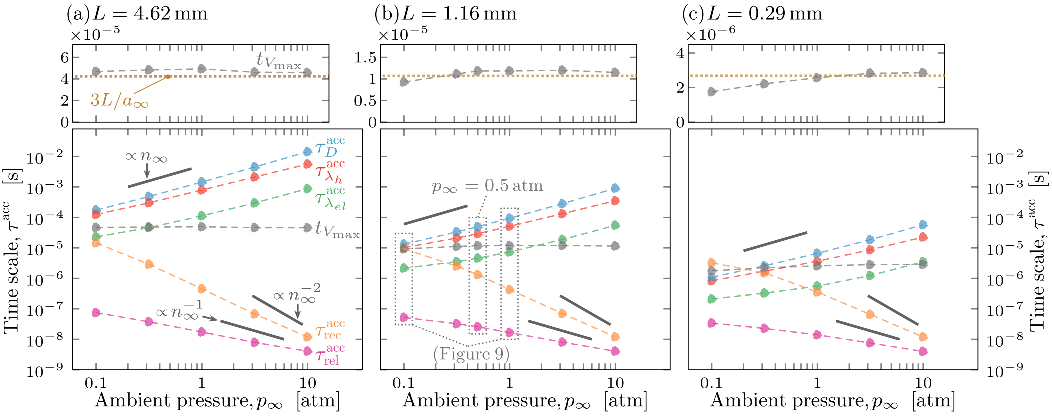

FIG. 5. Timescales from Table II accumulated according to (29) for $T_0 = 30\,000$ K and initial diameter (a) $L = 4.62$ mm, (b) $L = 1.16$ mm, and (c) $L = 0.29$ mm. The expansion time $t_{V_{\max}}$ is also shown above on a linear scale. The $L = 1.16$ mm kernel in (b) has initial volume matching that of all cases in Sec. V.

(Sec. V). The greater decrease in temperature for smaller kernels is also consistent with more rapid diffusion (e.g., Fig. 6).

Recombination is fast at higher pressures but slows with decreasing pressure as collision rates decrease. Although exact scaling is not expected due to temporal and spatial averaging and coupling between processes, it is approximately $\tau_{\mathrm{rec}}^{\mathrm{acc}} \propto n_\infty^{-2} \propto n_e/\mathcal{R}_1$ from (12) [e.g., Fig. 5(a)]. The heat released by electron recombination is expected to influence the expansion when $\tau_{\mathrm{rec}}^{\mathrm{acc}} \lesssim t_{V_{\max}}$, with its effect more pronounced for faster $\tau_{\mathrm{rec}}^{\mathrm{acc}}$; this is discussed in detail in Sec. IV. The value of $\tau_{\mathrm{rec}}^{\mathrm{acc}}$ decreases modestly with decreasing L because the recombination chemistry couples with electron thermal conduction, which is stronger for smaller L: rapid T_e decrease by diffusion drives the plasma further from $T_s = T_e$ chemical equilibrium (Fig. 6), which in turn accelerates recombination.

IV. EFFECT OF RECOMBINATION ON THE PLASMA EXPANSION

Based on the timescale analysis of the spherical case, we analyze the plasma expansion and subsequent hydrodynamic development for an asymmetric $L = 2$ mm kernel [matching an $L = 1.16$ mm spherical volume; Fig. 5(b)] with $p_\infty = 0.5$ atm. At these conditions, electron recombination is faster than the expansion, so the thermal energy released is anticipated to couple with it.

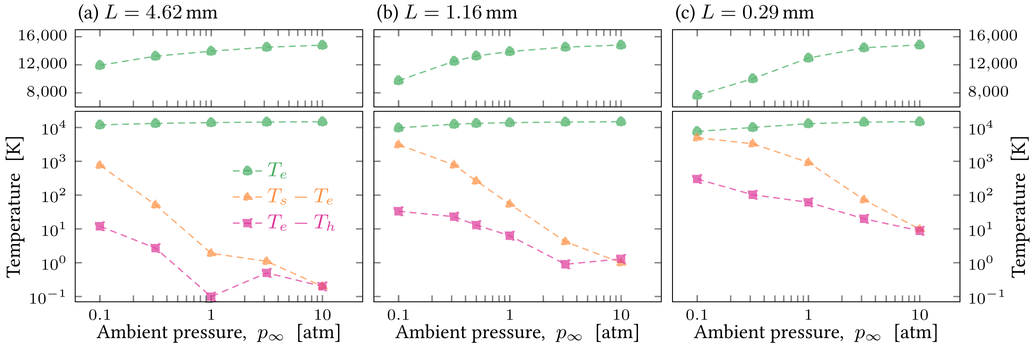

FIG. 6. Temperatures T_e, $T_s - T_e$ (25), and $T_e - T_h$ at $t = t_{V_{\max}}$ and $r = 0$ for (a) $L = 4.62$ mm, (b) $L = 1.16$ mm, and (c) $L = 0.29$ mm, corresponding to the cases shown in Fig. 5. The electron temperature T_e is also shown on a linear scale.

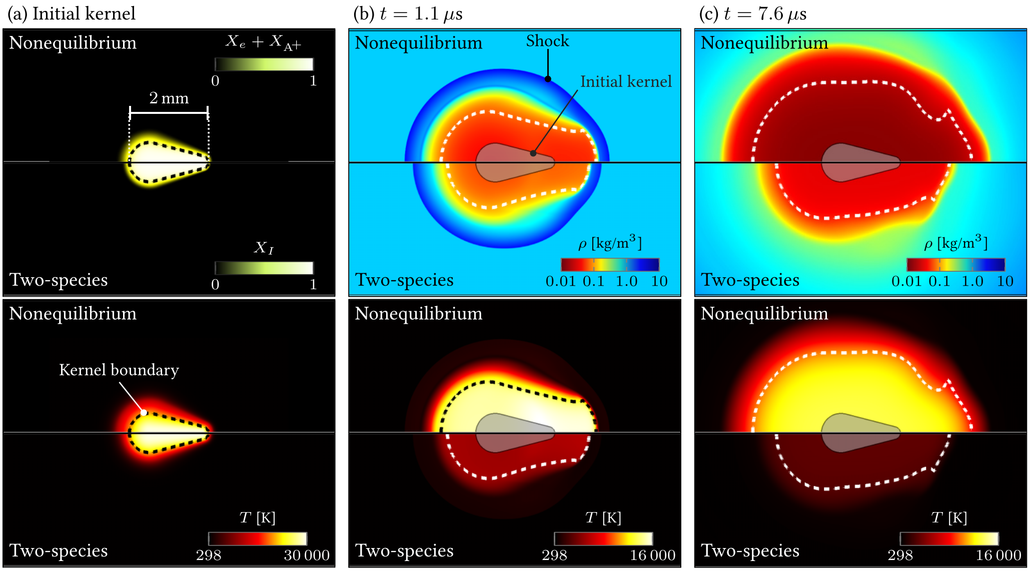

FIG. 7. An $L = 2$ mm, $T_0 = 30\,000$ K deposition in $p_\infty = 0.5$ atm argon at (a) its initial state, (b) $t = 1.1\,\mu$s, and (c) $t = 7.6\,\mu$s, computed using the nonequilibrium and two-species models as labeled. Dashed lines denote the kernel boundary, defined by $\xi = 0$ (24). Note the change in temperature scale.

This stage of the development will be shown in Sec. V to go on to produce the vortical structures that constitute the late-time ejection.

Matching the parameters in Sec. III, the post-breakdown plasma kernel has initial peak temperature $T_0 = 30\,000$ K and electron mole fraction $X_e = 0.489$. Its total energy is $E_0 = 48.5$ mJ, which is similar to experiments [3]. Its geometry $\alpha = 2$ and $\beta = 3$ (21) produced a pronounced ejection in previous inert-gas studies [9], also similar to that observed in experiments (e.g., Fig. 1).

A significant difference between the nonequilibrium and two-species cases, seen in the visualizations of Figs. 7(b) and 7(c) and in the time trace in Fig. 8(a), is that the temperature for the nonequilibrium model decays more slowly than for the two-species model. Another difference is that the plasma kernel expands to 2.8 times greater volume [Fig. 8(c)]. The main cause of these differences is heat release by electron recombination. The net formation energy of ions $E_f = \int \rho e_f\, d^3\boldsymbol{x}$ is 58% of total energy deposited. Recombination recovers this ionization energy by converting it to the translational energy of free electrons via the $-I_A \dot{n}_{e,1}$ term in (4). A portion of this is also subsequently transferred to heavy particles through elastic collisions. This increase in translational energy corresponds to the elevated kernel pressure and temperature seen in Figs. 8(a) and 8(b). Thus recombination is the primary cause of the enhanced plasma expansion. Sharp distortion of the kernel boundary [Fig. 7(c)] is due to a rotational flow being established at the smaller R_2 end of the kernel. In a single-fluid model this is observed to occur at the small R_2 end before the corresponding opposite-sign vorticity is generated near the larger R_1 end [9].

The effect of recombination on the expanded volume is quantified in Fig. 9 for $T_0 \in [15\,000\text{ K}, 61\,000\text{ K}]$ for a spherically symmetric kernel with initial diameter $L = 1.16$ mm, matching the volume of that in Fig. 7(a). The expansion is driven by the high kernel pressure, which we quantify with

$$\overline{p} = k_b\left(\frac{\overline{\rho Y_e}}{m_e}\overline{T}_e + \frac{\overline{\rho Y_{A^+}}}{m_{A^+}}\overline{T}_h + \frac{\overline{\rho Y_A}}{m_A}\overline{T}_h\right) \tag{30}$$

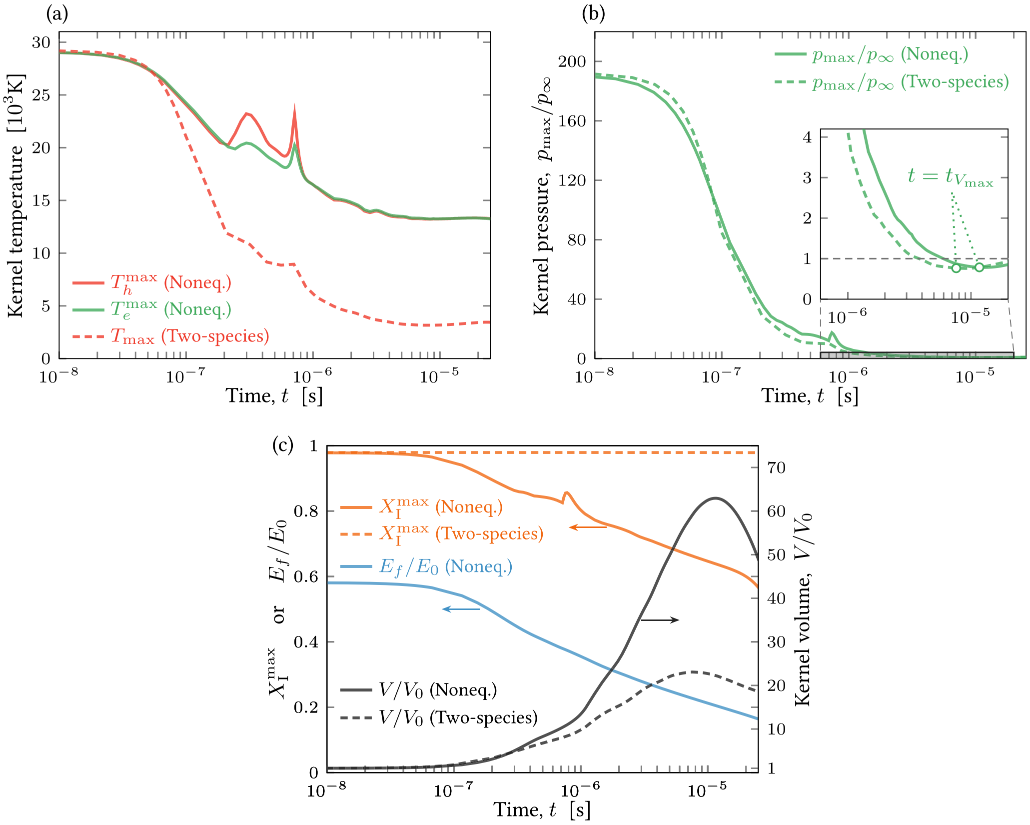

FIG. 8. Evolving kernel properties for the case shown in Fig. 7. V_0 is the initial volume of the kernel, and "max" refers to the peak value inside the kernel. Increases in $T^{\max}$, $p_{\max}$, and $X_I^{\max}$ result from transient kernel dynamics.

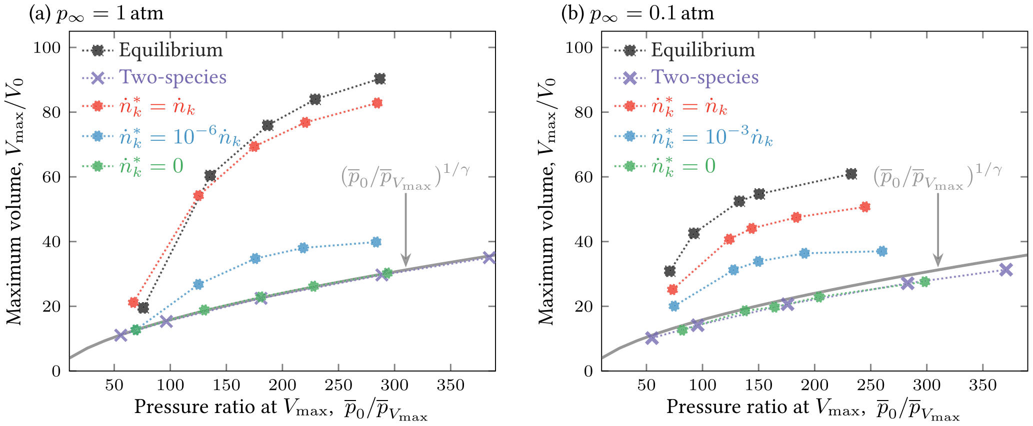

FIG. 9. Maximum volume $V_{\max}$ attained by a spherically symmetric $L = 1.16$ mm kernel for (a) $p_\infty =$ 1 atm and (b) $p_\infty = 0.1$ atm for a range of scaled $\dot{n}_k^* \leqslant \dot{n}_k$. The range of $\overline{p}_0/\overline{p}_{V_{\max}}$ corresponds to initial peak temperatures $T_0 \in [15\,000$ K, $61\,000$ K$]$.

based on mean kernel properties $\overline{T}_h$ (26), $\overline{T}_e$ (27), and $\overline{\rho Y_k}$ (28). For each T_0, the kernel pressure at its maximum volume $V_{\max}$ is denoted by $\overline{p}_{V_{\max}}$, and $\overline{p}_0$ is its initial pressure. In all cases, $\overline{p}_{V_{\max}} < p_\infty$ due to this radial expansion [7,9,56,59]; this is also seen in the Fig. 8(b) inset for the axisymmetric case. Dependence on the recombination rate is assessed by replacing the chemical source term $\dot{n}_k$ in (4) and (5) with a scaled $\dot{n}_k^* \leqslant \dot{n}_k$ (Fig. 9). For $\dot{n}_k^* = \dot{n}_k$, the kernel expands to a volume greater than that predicted by the two-species model. This enhancement is more pronounced at larger pressure ratio $\overline{p}_0/\overline{p}_{V_{\max}}$ due to the greater initial electron concentration at higher T_0. It is weaker for $p_\infty = 0.1$ atm [Fig. 9(b)] due to the decreased collision rate at lower number densities, consistent with the slower $\tau_{\mathrm{rec}}^{\mathrm{acc}}$ overlapping with $t_{V_{\max}}$ in Fig. 5(b). A similar enhancing effect has been reported for solid-surface laser ablation, but for much lower pressure (40 Pa) and resulting from metal rather than gaseous ions [46].

For $p_\infty = 1$ atm, $\dot{n}_k^* = 0$ results in an essentially adiabatic expansion from the initial kernel state to its maximum volume:

$$\frac{V_{\max}}{V_0} = \left(\frac{\overline{p}_0}{\overline{p}_{V_{\max}}}\right)^{1/\gamma}$$

with $\gamma = 5/3$. This matches the behavior of the two-species model. A similar trend occurs for $p_\infty = 0.1$ atm [Fig. 9(b)], though both the nonequilibrium model with $\dot{n}_k^* = 0$ and the two-species model depart slightly from adiabaticity due to enhanced thermal diffusivity in lower-density gas. The close match in $V_{\max}$ with the two-species model, which does not include electron thermal conduction, further suggests that heavy-particle thermal conduction, rather than that of electrons, primarily leads to this mild suppressing effect on the expansion. This is consistent with the overlap of $\tau_{\lambda_h}^{\mathrm{acc}}$ and $t_{V_{\max}}$ at $p_\infty = 0.1$ atm in Fig. 5.

These results are also compared to that of an equilibrium model, corresponding to the limiting case in which thermal and chemical equilibration are assumed to occur infinitely fast. In this single-temperature model with $T_e = T_h$, the composition is determined by the Saha relation (25) with $T_s = T_e$. The equilibrium kernel attains a greater expanded volume for nearly all cases in Fig. 9 because the recombining electrons instantly adjust to the decreasing T and ρ, thereby heating the gas at a rate faster than any of the finite-$\dot{n}_k$ cases. The slightly smaller volume for the low-energy $p_\infty = 1$ atm case, for which recombination plays a comparatively smaller role, is due to hydrodynamic-driven fluctuations in the instantaneous values of V and $\overline{p}$. The data in Fig. 9 indicate that finite-rate chemistry is necessary for quantitative prediction of the plasma expansion.

V. EFFECT ON EJECTION

To examine how these plasma mechanisms during the expansion affect the subsequent hydrodynamic ejection, we focus on vorticity generation [9]. As shown in Fig. 10, this occurs primarily during the plasma expansion; the net circulation

$$\Gamma = \iint \omega \, dx \, dr, \quad \text{where} \quad \omega = \frac{\partial u_r}{\partial x} - \frac{\partial u_x}{\partial r}, \tag{31}$$

varies only slowly after $t_{V_{\max}}$. Both models predict the most intense vorticity at the smaller R_2 end [Fig. 11(a)]. While there is greater negative circulation for the nonequilibrium case at $t_{V_{\max}}$ (Fig. 10), the vorticity is more diffuse and distributed over a larger volume [Fig. 11(a)]. The baroclinic torque [Fig. 11(c)] that generates it results from misalignment between the density gradient at the kernel boundary (due to low density of the expanding plasma) and the decreasing pressure that manifests as a gradient in the postshock rarefaction. This is the primary vorticity-generating mechanism for both models [Fig. 11(c)] and corresponds to the schematic in Fig. 1(b); detailed analysis of this hydrodynamic mechanism is reported elsewhere [9]. In contrast to the simple $\mu \propto T^{0.7}$ viscosity of the two-species model (16), the viscosity for the nonequilibrium case [Fig. 11(b)] is low inside the kernel due to free electrons. While high viscosity along its perimeter contributes to the diffuse ω distribution seen in Fig. 11(a), it will be shown insufficient by itself to cause this.

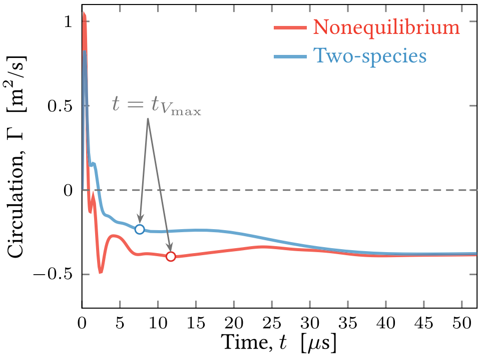

FIG. 10. Circulation (31) time evolution for the nonequilibrium and two-species models, with $T_0 =$ 30 000 K and $t_{V_{\max}}$ as indicated.

The negative vorticity auto-advects subsonically in the negative-x direction and penetrates the hot plasma (Fig. 12). For the two-species model this vorticity is concentrated near $r = 0$ and breaches the opposite side of the kernel by $t = 52\,\mu$s [Fig. 12(b)]. In contrast, for the nonequilibrium model the more diffuse vorticity is located at a greater r distance and advects slowly [Fig. 12(a)].

To analyze mechanisms that lead to the weakened, diffuse ejection seen in Fig. 12(a), we seek to isolate the effects of plasma-expansion enhancement, viscosity, and thermal conduction. First, the initial temperature for the two-species model is elevated to $T_0 = 155\,000$ K so that the peak kernel volume matches (to within 8%) that of the nonequilibrium model. As seen in Fig. 13(b), the vorticity is still concentrated near the centerline and advects rapidly, similar to that in Fig. 12(b), indicating the recombination-enhanced expansion alone is insufficient to weaken the ejection.

To assess the effect of viscosity, the $\mu \propto T^{0.7}$ model (16) is replaced by a uniform $\mu = 6\mu_\infty$ to match the peak viscosity of the nonequilibrium model at $t_{V_{\max}}$ [Fig. 11(c)]. As shown in Fig. 13(c), even this large increase does not reproduce the slowly advecting, diffuse vorticity of the nonequilibrium model, which occurs despite the low viscosity inside the plasma kernel [Fig. 11(b)]. The similar vorticity distributions [Figs. 13(b) and 13(c)] and circulation time traces (Pr = 0.66 curves; Fig. 14) also indicate that using an appropriately selected uniform viscosity instead of $\mu \propto T^{0.7}$ does not significantly alter the ejection during this early formation stage.

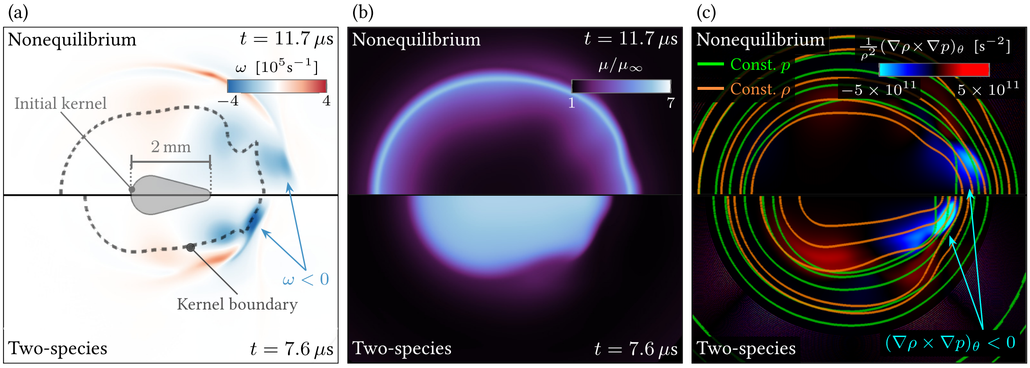

FIG. 11. (a) Vorticity and (b) viscosity at $t_{V_{\max}}$ for the nonequilibrium model ($t_{V_{\max}} = 11.7\,\mu$s) and the two-species model ($t_{V_{\max}} = 7.6\,\mu$s), corresponding to the cases shown in Fig. 7. (c) Azimuthal baroclinic torque overlaid with $p/p_\infty \in [0.85, 1.26]$ and $\rho/\rho_\infty \in [0.02, 0.90]$ contours, averaged over $t/t_{V_{\max}} \in [0.3, 1.0]$. The kernel boundary in (a) is defined by $\xi = 0$ (24).

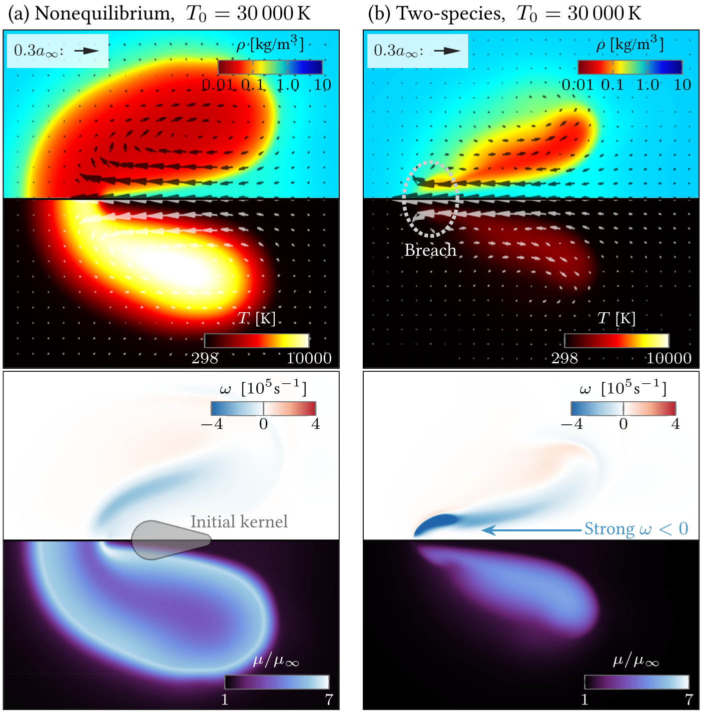

FIG. 12. Flow at $t = 52\ \mu$s for the (a) nonequilibrium model and (b) two-species model for $T_0 = 30\,000$ K, corresponding to cases shown in Fig. 7. The velocity vector scale is given in terms of the ambient speed of sound. The initial kernel is shown in gray in (a).

Due to the high thermal conductivity and low viscosity of electrons, the Prandtl number of the plasma can differ significantly from the constant Pr = 0.66 approximation used for the two-species model. For example, at $t_{V_{\max}} = 11.7\ \mu$s the thermal conductivity $\lambda_h + \lambda_{el}$ is 32 times higher at the kernel center than in the ambient gas, and the Prandtl number of the plasma varies significantly: $\mathrm{Pr} = c_p\mu/(\lambda_h + \lambda_{el}) \in [0.04, 0.66]$. To assess the effect of this enhanced conductivity, a uniform Pr = 0.17 is used for the two-species model. As shown in Fig. 13(d), this leads to weaker, more

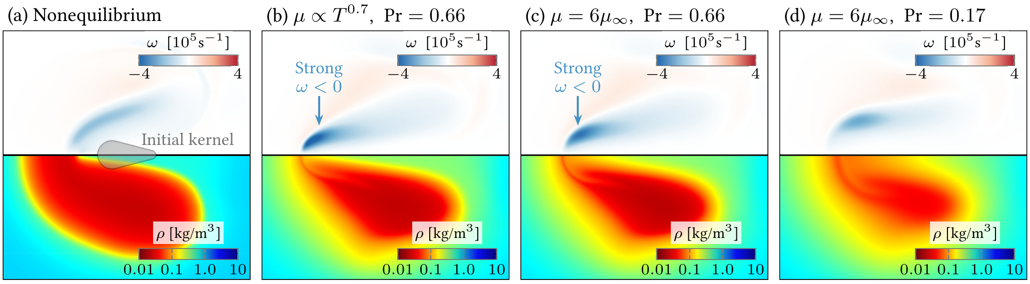

FIG. 13. Flow at $t = 52\ \mu$s for (a) the nonequilibrium model with $T_0 = 30\,000$ K, and the two-species model with $T_0 = 155\,000$ K and various transport models: (b) $\mu \propto T^{0.7}$ viscosity (16), (c) uniform $\mu = 6\mu_\infty$, and (d) uniform $\mu = 6\mu_\infty$ with Pr = 0.17.

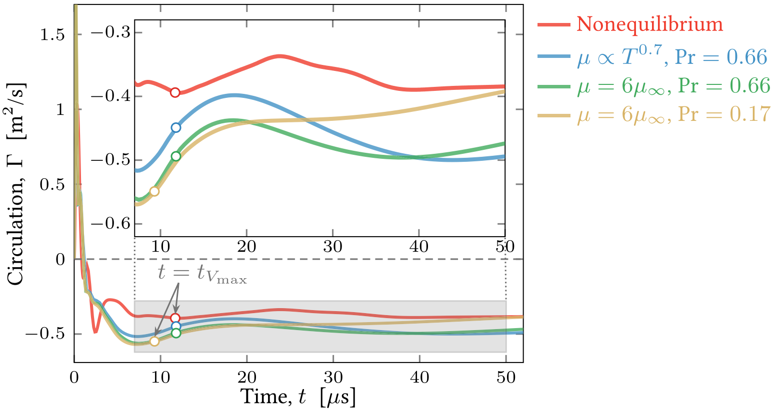

FIG. 14. Circulation (31) for the nonequilibrium model with $T_0 = 30\,000$ K and the two-species model with $T_0 = 155\,000$K and various transport models, corresponding to cases shown in Fig. 13.

diffuse vorticity located farther from the centerline, suggesting that the similar distribution seen in the nonequilibrium case [Fig. 13(a)] also results in part from large thermal conductivity.

Coupling between thermal conduction and the plasma expansion would be consistent with the timescales of Fig. 5(b), which indicates that for $p_\infty = 0.5$ atm, both $\tau^{\mathrm{acc}}_{\lambda_h}$ and $\tau^{\mathrm{acc}}_{\lambda_{el}}$ are comparable to $t_{V_{\max}}$. Decreasing Pr = 0.66 to Pr = 0.17 does not significantly change the net circulation (31) generated during the expansion ($\mu = 6\mu_\infty$ curves for $t \leqslant t_{V_{\max}}$; Fig. 14), but it can alter the distribution due to thickening of temperature, and thus density gradients, which in turn weakens baroclinic torque. Following the expansion, the (negative) circulation for Pr = 0.17 diverges from Pr = 0.66 and decreases as the vorticity advects into the plasma, consistent with the weaker penetration seen at $t = 52\,\mu$s [Fig. 13(d)]. This indicates that suppression of the ejection results from mechanisms occurring during both the expansion and subsequent vortex-advection stages. The low Prandtl number alone, however, is insufficient to suppress the ejection; $\mu = \mu_\infty$, Pr = 0.17 does not reproduce the distribution seen in Fig. 13(d). This indicates that the observed weakened ejection in a plasma is due to the combined diffusive effects of both viscosity and thermal conduction.

VI. CONCLUSIONS

A two-temperature, three-species argon-plasma model is used to quantify post-breakdown timescales for diffusion, thermal relaxation, and electron recombination to determine conditions for which these might couple with the hydrodynamics. Direct thermal-nonequilibrium effects are found to be weak because of their fast relaxation timescales and would seem to require lower pressures ($p_\infty \lesssim 0.01$ atm) or smaller kernels ($L \lesssim 0.1$ mm) than reported, and even then the breakdown-induced flow would be suppressed by viscosity and diffusion. In contrast, chemical nonequilibrium plays an important role: recombination enhances the plasma expansion by heating the gas with the stored ionization energy. This occurs for $p_\infty \in [0.1\ \text{atm},\ 10\ \text{atm}]$ and is more pronounced at higher pressure due to rapid collision rates. At low pressure thermal conduction is shown to mildly suppress the expansion. Comparison with inert-gas simulations confirm that thermal conduction, enhanced by free electrons, also leads to a more diffuse vorticity distribution, which slows its penetration into the plasma kernel and weakens the ultimate ejection. These results point to important mechanisms to consider and means of tailoring breakdowns for different purposes. They are also a first step toward including models for more complex chemistry and intersections with particles, droplets, or interfaces.

ACKNOWLEDGMENTS

We thank Jon E. Retter and Gregory S. Elliott for providing experimental images of the post-breakdown evolution. We are also grateful to Alessandro Munafó and Andrea Alberti for helpful discussions. This material is based in part upon work supported by the Department of Energy, National Nuclear Security Administration, under Award No. DE-NA0002374.

APPENDIX A: NONEQUILIBRIUM PLASMA MODEL

The submodels used to close the governing equations (1)–(6) are presented here. The internal energy $e = e_f + e_h + e_e$ in (3) includes the formation, heavy-particle, and electronic energies:

$$e_f = Y_A^+ \frac{I_A}{m_{A^+}}, \quad e_h = \frac{3}{2}\left(\frac{Y_A}{m_A} + \frac{Y_{A^+}}{m_{A^+}}\right) k_b T_h, \quad \text{and} \quad e_e = \sum_k Y_k e_{e,k}. \tag{A1}$$

The electronic energy e_e includes both translation energies of free electrons and the excitation of heavy species to a single energy level ε_k, so the electronic energy $e_{e,k}$ of the kth species is [28]

$$e_{e,e} = \frac{3}{2}\frac{k_b T_e}{m_e} \quad \text{and} \quad e_{e,k} = \frac{g_k^1 \exp\left(-\frac{\varepsilon_k}{k_b T_e}\right)}{g_k^0 + g_k^1 \exp\left(-\frac{\varepsilon_k}{k_b T_e}\right)} \frac{\varepsilon_k}{m_k} \quad \text{for} \quad k \in \{A, A^+\}, \tag{A2}$$

where g_k^l is the degeneracy of the lth energy level for the kth species (see Table III for argon values used).

For A and A^+ the electronic enthalpy $h_{e,k}$ is equal to $e_{e,k}$ (A2), and for electrons $h_{e,e} = e_{e,e} + k_b T_e / m_e$ [27]. The Wilke mixture rule is used to compute the dynamic viscosity μ in (7) [61]. The heavy-particle thermal conductivity λ_h in (8) is computed assuming no electron-ion interaction, resulting in $\lambda_h = X_A \lambda_A$ [34]. Similarly, only the free-electron contribution is included in $\lambda_{el} = X_e \lambda_e$. The species viscosity, species thermal conductivity, and binary diffusion coefficients are represented with established models [35]:

$$\mu_k = \frac{5}{16}\frac{\sqrt{\pi m_k k_b T}}{\overline{Q}_{kk}^{(2,2)}}, \quad \lambda_k = \frac{15}{4}\frac{k_b}{m_k}\mu_k, \quad \text{and} \quad \mathcal{D}_{kl} = \frac{3}{8}\frac{k_b T}{p}\sqrt{\frac{\pi k_b T (m_k + m_l)}{2 m_k m_l}}\frac{1}{\overline{Q}_{kl}^{(1,1)}}, \tag{A3}$$

where $T = T_e$ for electron properties and electron-heavy interactions, and $T = T_h$ otherwise. Rapid diffusion of free electrons, which would produce charge separation, is counteracted by a locally induced electric field, resulting in electrons and ions diffusing in tandem [32]. This ambipolar diffusion, which suppresses free-electron diffusion and enhances ion diffusion, is modeled with standard expressions, appropriately simplified for a three-component mixture [31]:

$$\boldsymbol{V}_e = \boldsymbol{V}_{A^+} = \left[-\frac{1}{X_e}\frac{W_A}{W} D_{\text{amb}} + \frac{W_A^2}{W^2}(D_{\text{amb}} - D_{\text{neut}})\right] \nabla X_e, \tag{A4}$$

$$\boldsymbol{V}_A = \left[\frac{1}{X_A}\frac{W_A}{W} D_{\text{neut}} + \frac{W_A^2}{W^2}(D_{\text{amb}} - D_{\text{neut}})\right] \nabla X_e, \tag{A5}$$

TABLE III. Degeneracies and energy levels for argon, grouped approximately [60].

	g_k^0	g_k^1	ε_k	I_k
A	1	12	11.5 eV	15.8 eV
A^+	6	2	13.5 eV	∞

where

$$D_{\mathrm{amb}} = 2\mathcal{D}_{AA^+}, \qquad D_{\mathrm{neut}} = 2\mathcal{D}_{AA^+}\left(1 - \frac{\mathcal{D}_{AA^+}}{D_{eA^+}}\right) \tag{A6}$$

and

$$D_{ij} = \mathcal{D}_{ij}\left[1 + \frac{n_k(\mathcal{D}_{ik}m_k/m_j - \mathcal{D}_{ij})}{n_i\mathcal{D}_{jk} + n_j\mathcal{D}_{ik} + n_k\mathcal{D}_{ij}}\right], \quad \text{for} \quad i, j, k \in \{A, A^+, e^-\} \quad \text{and} \quad i \neq j \neq k.$$

As crafted, the diffusion velocities (A4)–(A5) ensure mass conservation ($\sum_k \rho Y_k \boldsymbol{V}_k = \boldsymbol{0}$) and are consistent with charge neutrality ($n_{A^+}\boldsymbol{V}_{A^+} = n_e\boldsymbol{V}_e$).

The collision integrals in (A3) are

$$\overline{Q}_{ij}^{(l,s)} = \frac{4(l+1)}{(s+1)!\,[2l+1-(-1)^l]}\int_0^\infty z^{2s+3}e^{-z^2}Q_{ij}^l(z)\,dz, \tag{A7}$$

where $Q_{ij}^l(z) \equiv 2\pi\int_0^\infty(1-\cos^l\chi)\,\sigma_{ij}(z,\chi)\sin\chi\,d\chi$ is the momentum-transfer cross section for $l = 1$ and viscosity cross section for $l = 2$ [22,28,35]; χ, g, and $\sigma_{ij}(z,\chi)$ correspond respectively to the collision scattering angle, relative velocity magnitude, and differential cross section, and

$$z^2 = \frac{m_i m_j g^2}{2k_bT(m_i + m_j)}.$$

A constant, representative value is used for $\overline{Q}_{AA^+}^{(1,1)} = 87.0$ Å^2, which is based on Chapman-Enskog calculations at $T = 10\,000$ K by Devoto [62] and includes the effect of charge-exchange reactions, and $\overline{Q}_{eA}^{(1,1)}$ is approximated by an established fit [63],

$$\overline{Q}_{eA}^{(1,1)} = \begin{cases}\left[0.713 - (4.5\times10^{-4}\ \mathrm{K}^{-1})T_e + (1.5\times10^{-7}\ \mathrm{K}^{-2})T_e^2\right]\times\text{Å}^2, & T_e < 3000\ \mathrm{K}\\ \left[-0.488 + (3.96\times10^{-4}\ \mathrm{K}^{-1})T_e\right]\times\text{Å}^2, & T_e \geqslant 3000\ \mathrm{K}.\end{cases} \tag{A8}$$

For interactions between electrons and ions, we use

$$\overline{Q}_{eA^+}^{(1,1)} = \frac{2\pi\epsilon^4}{9(k_bT_e)^2}\log\left[\frac{9k_b^3T_e^3}{4\pi\epsilon^6 n_e}\right], \tag{A9}$$

where $\epsilon^2 \equiv k_e q_e^2$, with $k_e = 8.987\times10^9$ Nm^2/C^2 the Coulomb constant and $q_e = 1.602\times10^{-19}$ C the electron charge [36]. For the neutral-particle interactions, we use an established fit [33]

$$\overline{Q}_{AA}^{(2,2)} = (170\ \mathrm{K}^{1/4})\,T_h^{-1/4}\times\text{Å}^2. \tag{A10}$$

These integrated cross sections (A8)–(A10) have been used to model hypersonic boundary layers and shocks in argon [33,36] and closely match detailed calculations by Devoto [62]. For charged particles, $\overline{Q}_{A^+A^+}^{(2,2)} = 1.36Q_c$ and $\overline{Q}_{ee}^{(2,2)} = 1.29Q_c$ include constants calibrated [35,64] to match theoretical calculations of transport properties in a fully ionized gas [65], where

$$Q_c = \frac{\epsilon^4}{(k_bT_e)^2}\log\left[\frac{9(k_bT_e)^3}{4\pi\epsilon^6 n_e} + \frac{16(k_bT_e)^2}{\epsilon^4 n_e^{2/3}}\right]^{1/2}.$$

The thermal relaxation time τ_{ek} in (4) due to elastic collisions between free electrons and heavy species k is [22]

$$\frac{1}{\tau_{ek}} = \frac{8}{3}\frac{m_e}{m_k}n_k\sqrt{\frac{8k_bT_e}{\pi m_e}}\,\overline{Q}_{ek}^{(1,1)}(T_e). \tag{A11}$$

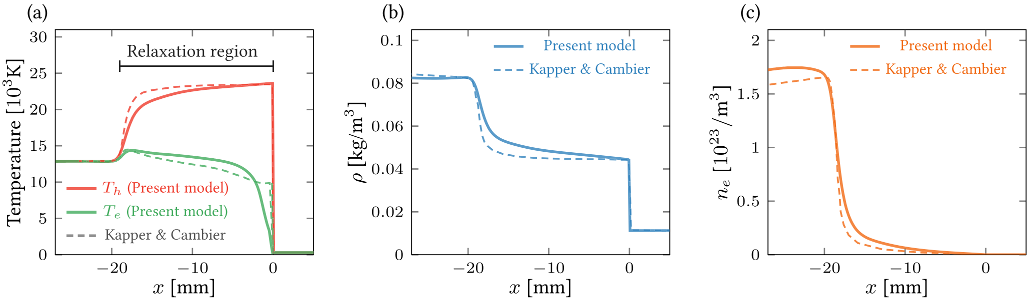

FIG. 15. Comparison of (a) temperatures, (b) density, and (c) electron number density for the present plasma model with the detailed model of Kapper and Cambier [54] for a Mach 15.9 shock in argon.

For the kinetics model, the rate constants $k_{f,1}$ and $k_{f,2}$ in (12) and (13) are based on those developed by Hoffert and Lien [37]:

$$k_{f,1} = (3.75 \times 10^{-16}\ \mathrm{K}^{-3/2})T_e^{3/2}\left(\frac{\mathcal{E}_A}{k_bT_e} + 2\right)\exp\left(-\frac{\mathcal{E}_A}{k_bT_e}\right) \times \mathrm{cm}^3/\mathrm{s}, \tag{A12}$$

$$k_{f,2} = (1.68 \times 10^{-20}\ \mathrm{K}^{-3/2})T_h^{3/2}\left(\frac{\mathcal{E}_A}{k_bT_h} + 2\right)\exp\left(-\frac{\mathcal{E}_A}{k_bT_h}\right) \times \mathrm{cm}^3/\mathrm{s}. \tag{A13}$$

The Saha equilibrium constant $K_{\mathrm{eq}}(T)$ in (12) and (13) is approximated with the first term of the electronic partition functions of A and A^+ [28,38], corresponding to their ground states:

$$K_{\mathrm{eq}}(T) = 2\frac{g^0_{A^+}}{g^0_A}\left(\frac{2\pi m_e k_b T}{h^2}\right)^{3/2} \exp\left(-\frac{I_A}{k_bT}\right). \tag{A14}$$

Because (A12) and (A13) assume excitation of the neutral particle A to be rate-controlling and is expected to be valid only for $T \geqslant 3000$ K [37], we use $T_{\mathrm{modified}} = \max(T,\ 3000\ \mathrm{K})$ when computing (A12) and (A13); a similar approach was taken by Liu *et al.* [33] to avoid large recombination rates at low temperatures. In the present analysis, recombination occurs predominantly by (10) in hot plasma where $T_e > 3000$ K, so it is unaffected by this choice.

APPENDIX B: VALIDATION: A MACH 15.9 SHOCK IN ARGON

The nonequilibrium model used is compared with the detailed two-temperature model of Kapper and Cambier [54], which, in addition to the physics included here, includes 31 atomic energy levels, photoionization, bound-bound electronic transitions, and bremsstrahlung emission. Figure 15 shows the Mach 15.9 shock structure in $T_\infty = 293.6$ K, $p_\infty = 685.3$ Pa argon. There is good agreement in the length of the relaxation region behind the shock front [Fig. 15(a)], which results from a competition between thermal relaxation and electron-impact ionization. The electron avalanche in the relaxation zone produces a free-electron spatial distribution which also agrees well [Fig. 15(c)]. Coupling between gas-dynamic rarefaction waves and the temperature-sensitive ionization avalanche causes an oscillation with period 31 μs, matching well the 32.5 μs predicted by Kapper and Cambier [66].

APPENDIX C: EFFECT OF RADIATION

Emissions due to free-free and bound-bound electronic transitions are modeled as

$$A^+ + e \to A^+ + e + h\nu, \tag{C1}$$

$$A(j) \to A(i) + h\nu, \tag{C2}$$

where ν is the frequency of the emitted photon. Free-bound radiation is anticipated to be weak based the calculations of Kapper and Cambier [54] and therefore not included here. For free-free transitions, or bremsstrahlung, all emitted radiation is assumed to escape the plasma, so the radiated power is [54,67]

$$\dot{Q}_{FF} = \frac{64\epsilon^6\pi^{3/2}}{3\sqrt{6}m_e^{3/2}hc^3}\bar{g}Z_{\mathrm{eff}}^2 n_e^2\sqrt{k_b T_e}, \tag{C3}$$

where c is the speed of light in vacuum, $\bar{g} = 1$ is the Gaunt factor, and $Z_{\mathrm{eff}}^2 = 1.67$ [68] is the effective nuclear charge.

Among bound-bound transitions, $4s$–$4p$ emissions by the neutral particle is anticipated to be strongest [69]; consistent with this, Kapper and Cambier [54] showed that including additional transitions results in only minor changes to the electron concentration behind a Mach 15.9 shock. Resonant emissions are assumed to be locally absorbed, whereas $4s$–$4p$ emissions are assumed to escape. The radiated power is modeled as [70]

$$\dot{Q}_{BB} = \sum_j n_A^j h\nu_j A_{j,j-1}, \tag{C4}$$

where A_j is the Einstein coefficient for the jth transition, ν_j is its emitted frequency, and n_A^j is the number density for the higher energy level of the transition assuming a Boltzmann distribution and $n_A = \sum_j n_A^j$:

$$n_A^j = n_A \frac{\tilde{g}_A^j \exp\left(-\tilde{\varepsilon}_A^j/k_b T_e\right)}{\sum_i \tilde{g}_A^i \exp\left(-\tilde{\varepsilon}_A^i/k_b T_e\right)}.$$

The excited energy level $\tilde{\varepsilon}_A^j$ is distinct from the approximately grouped ε_A of the thermodynamic model (Table III). Grouping is not employed for the radiation model due to variation of $A_{j,j-1} \in [10^3\ \mathrm{s}^{-1},\ 4.5\times 10^7\ \mathrm{s}^{-1}]$ and $h\nu_j \in [1.08\ \mathrm{eV},\ 1.86\ \mathrm{eV}]$, based on data by Wiese *et al.* [71], so all 30 reported $4s-4p$ transitions are used, and $\tilde{\varepsilon}_A^j$ is taken from Kramida *et al.* [60].

The total radiated power $\dot{Q}_{\mathrm{rad}} = \dot{Q}_{FF} + \dot{Q}_{BB}$ is included in the governing equations for total and electronic energy as follows:

$$\frac{\partial \rho(e + |\boldsymbol{u}|^2/2)}{\partial t} + \nabla\cdot[\rho(e + |\boldsymbol{u}|^2/2)\boldsymbol{u}] + \nabla\cdot[(p\boldsymbol{I} - \boldsymbol{\tau})\boldsymbol{u}] + \nabla\cdot\boldsymbol{q} = -\dot{Q}_{\mathrm{rad}},$$

$$\frac{\partial \rho e_e}{\partial t} + \nabla\cdot\rho e_e\boldsymbol{u} + \nabla\cdot p_e\boldsymbol{u} + \nabla\cdot\boldsymbol{q}_e = \boldsymbol{u}\cdot\nabla p_e + \frac{3}{2}n_e k_b(T_h - T_e)\left(\frac{1}{\tau_{eA^+}} + \frac{1}{\tau_{eA}}\right) - I_A\dot{n}_{e,1} - \dot{Q}_{\mathrm{rad}}.$$

Figure 16 shows the effect of radiation on the plasma expansion. Radiative loss is most pronounced at $p_\infty = 10$ atm, due in part to greater electron number density, and decreases V_{max} by 15% [Fig. 16(c)]. The electron mole fraction X_e at $t_{V_{\mathrm{max}}}$ is also 49% lower due to the lower temperature. Though the radiation directly affects only T_e, deviation between T_h and T_e remains negligible due to rapid thermal relaxation at high pressure.

For conditions of primary interest ($p_\infty \lesssim 1$ atm), the effect of radiation is negligible, as seen in Figs. 16(a) and 16(b). Even at $p_\infty = 10$ atm, the radiation-driven decrease in temperature and X_e is verified to have a negligible effect on the timescales in Fig. 5.

APPENDIX D: VALIDATION: T_e-FILTER AND $X_{e,\infty}$ INSENSITIVITY

The stabilizing filter for electron thermal conduction and $X_{0,\infty}$ modeling choices are shown here to leave results essentially unchanged. The T_e filter is second-order:

$$\hat{f}_j = \tfrac{1}{2}f_j + \tfrac{1}{4}(f_{j+1} + f_{j-1}). \tag{D1}$$

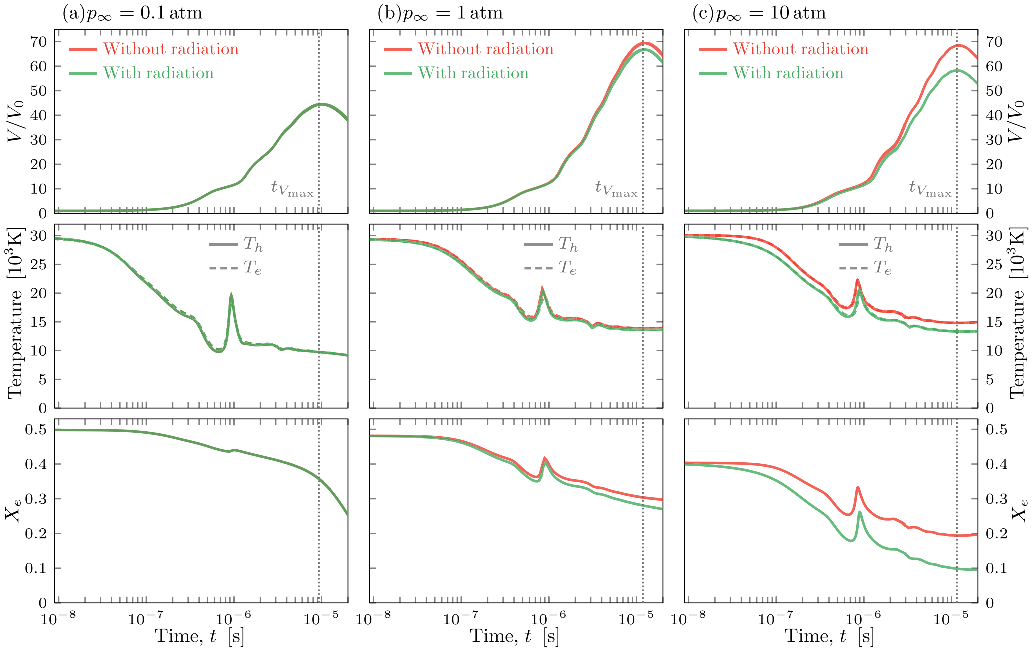

FIG. 16. Effect of radiation on kernel volume V, temperatures T_h and T_e, and electron mole fraction X_e, taken at $r = 0$, for an $L = 1.16$ mm spherical kernel with (a) $p_\infty = 0.1$ atm, (b) $p_\infty = 1$ atm, and (c) $p_\infty = 10$ atm. Note that $T_h \approx T_e$ for these cases.

It is applied four times to $\nabla \cdot (\lambda_{el} \nabla T_e)$ for each evaluation; the corresponding transfer function [48] is compared in Fig. 17 to those of the eighth-order explicit filter

$$\hat{f}_j = \frac{93}{128} f_j + \frac{7}{32}(f_{j+1} + f_{j-1}) - \frac{7}{64}(f_{j+2} + f_{j-2}) + \frac{1}{32}(f_{j+3} + f_{j-3}) - \frac{1}{256}(f_{j+4} + f_{j-4}) \tag{D2}$$

and implicit filter [72]

$$\hat{f}_j + \alpha_f(\hat{f}_{j+1} + \hat{f}_{j-1}) = \frac{93 + 70\alpha_f}{128} f_j + \frac{7 + 18\alpha_f}{32}(f_{j+1} + f_{j-1}) + \frac{-7 + 14\alpha_f}{64}(f_{j+2} + f_{j-2}) + \frac{1 - 2\alpha_f}{32}(f_{j+3} + f_{j-3}) + \frac{-1 + 2\alpha_f}{256}(f_{j+4} + f_{j-4}), \tag{D3}$$

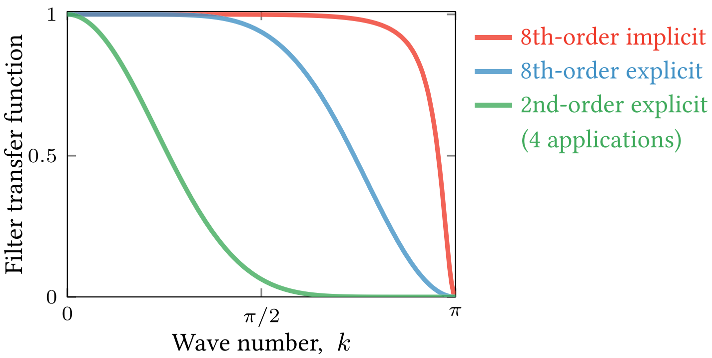

FIG. 17. Filter transfer function for eighth-order explicit (D2) and implicit (D3) filters, and four applications of a second-order explicit filter (D1).

TABLE IV. Cases used to test sensitivity to the filter and $X_{e,\infty}$. For all cases, the mesh spacing is $\Delta r = 1.4\,\mu$m.

Case	$\nabla \cdot (\lambda_{el} \nabla T_e)$ filter	$X_{e,\infty}$
1	Yes	10^{-8}
2	No	10^{-8}
3	No	10^{-12}

with $\alpha_f = 0.495$, which are applied to the solution variables (see Sec. II D).

Insensitivity to this intentionally aggressive second-order filter as well as choice of $X_{e,\infty} = 10^{-8}$ is verified with one-dimensional simulations of a spherically symmetric $L = 1.16$ mm, $T_0 = 30\,000$ K kernel with $p_\infty = 0.5$ atm, which present similar resolution challenges as all the cases considered herein. Table IV summarizes the parameters used, and Fig. 18 compares the results at $t_{V_{\max}} = 11.5\,\mu$s. The data for cases 1 and 2 collapse to plotting accuracy.

Case 3 with $X_{e,\infty} = 10^{-12}$ exhibits minor departure from cases 1 and 2 at the perimeter of the kernel, where there is a small peak in T_e. The feature itself does not result from the filter or $X_{e,\infty}$, and it does not depend on mesh resolution. It occurs in a region where both the electron concentration [Fig. 18(c)] and electronic energy are small (Fig. 19), and where thermal relaxation with heavy particles is very slow. It is unclear whether this feature would manifest at these conditions using a more detailed plasma model, though seemingly similar thermal nonequilibrium in cold gas can occur in plasma-arc simulations [73,74]. An artificial increase in relaxation rate was employed in those cases to suppress this nonequilibrium, though for this work the relaxation rates in (A11) are unmodified. It is unlikely this small feature affects results: despite the apparent change in T_e, it is energetically weak, as only trace electrons are available to carry the electronic energy, which monotonically decreases (Fig. 19).

APPENDIX E: VALIDATION: Δt INSENSITIVITY

Insensitivity to Δt is confirmed using spherically symmetric simulations for the range of p_∞ and L analyzed in Sec. III. Table V shows the relative change, such as $\Delta T_h/T_h$, in relevant quantities for simulations in which the time step Δt is decrease by a factor of 4 relative to that use in the analysis. In all cases, this has a negligible effect on results.

APPENDIX F: TIMESCALE FORMULATIONS

The timescales listed in Table II are formulated based on mean kernel properties (26)–(28). For the electron diffusion timescale τ_D, the kernel radius R is chosen as the relevant length, and $\overline{D}_{\text{amb}} =$

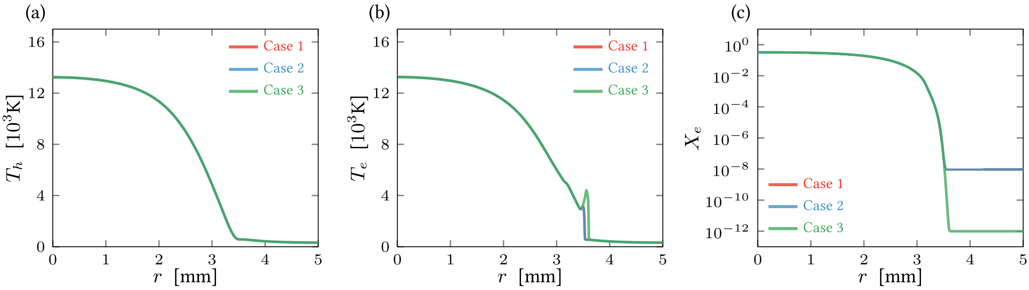

FIG. 18. Comparison at $t_{V_{\max}} = 11.5\,\mu$s of (a) T_h, (b) T_e, and (c) X_e for a spherically symmetric $L = 1.16$ mm kernel for $T_0 = 30\,000$ K and $p_\infty = 0.5$ atm; cases are described in Table IV.

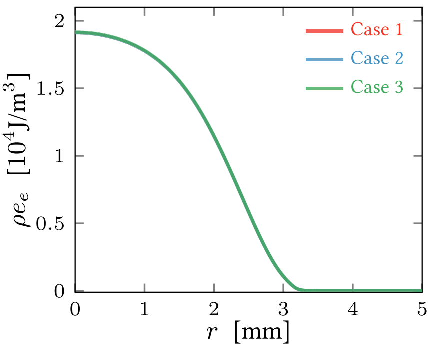

FIG. 19. Comparison at $t_{V_{\max}} = 11.5\,\mu$s of ρe_e for the cases in Table IV.

$D_{\mathrm{amb}}(\overline{T}_h)$ (A6) is the ambipolar diffusion coefficient evaluated with $\overline{T}_h$ (26). The nominal kernel mean molecular weight $\overline{W} = \overline{\rho}/\overline{C}$ is calculated from

$$\overline{\rho} = \frac{1}{V}\int_{\mathcal{V}} \rho\, d^3\boldsymbol{x} \quad \text{and} \quad \overline{C} = \frac{1}{V}\int_{\mathcal{V}} \frac{n}{\mathcal{N}}\, d^3\boldsymbol{x}, \tag{F1}$$

where $\mathcal{N}$ is the Avogadro constant. As R, $\overline{W}$, and $\overline{D}_{\mathrm{amb}}$ evolve, the timescale τ_D is an estimate of the evolving rate of electron diffusion. For a constant-R, constant-coefficient, linear diffusion system [75] with diffusion velocity $\boldsymbol{V}_e$ (A4), τ_D is the time scale for all gradients to be smoothed.

Thermal diffusion scales τ_{λ_h} and $\tau_{\lambda_{el}}$ (Table II) are analogously defined and based on the heavy-particle-translational and free-electron thermal diffusivities, $\overline{\lambda}_h/\overline{\rho}\,\overline{c}_p^t$ and $\overline{\lambda}_{el}/\overline{\rho}\,\overline{c}_p^e$, respectively. For these estimates, the conductivities $\overline{\lambda}_h = \lambda_h(\overline{T}_h, \overline{X}_A)$ and $\overline{\lambda}_{el} = \lambda_{el}(\overline{T}_e, \overline{X}_e)$ are evaluated with mean kernel temperatures and $\overline{X}_k = \overline{n}_k/\overline{n}$, where

$$\overline{n}_k = \frac{1}{V}\int_{\mathcal{V}} n_k\, d^3\boldsymbol{x} \quad \text{and} \quad \overline{n} = \frac{1}{V}\int_{\mathcal{V}} n\, d^3\boldsymbol{x}. \tag{F2}$$

The corresponding specific heats are

$$\overline{c}_p^t = \sum_{k\in\{A,A^+\}} \frac{\overline{\rho Y_k}}{\overline{\rho}} \frac{5}{2}\frac{k_b}{m_k} \quad \text{and} \quad \overline{c}_p^e = \sum_k \frac{\overline{\rho Y_k}}{\overline{\rho}} \frac{\partial h_{e,k}}{\partial T_e}\bigg|_{\overline{T}_e}.$$

Together, τ_{λ_h} and $\tau_{\lambda_{el}}$ are the timescales for the kernel size R to attain uniform temperature by heavy-particle and electron thermal conduction.

For recombination, τ_{rec} is computed from kernel-integrated recombination rates based on (12) and (13):

$$\overline{\mathcal{R}}_{1,b} = \frac{1}{V}\int_{\mathcal{V}} \frac{k_{f,1}}{K_{\mathrm{eq}}(T_e)} n_e^2 n_{A^+}\, d^3\boldsymbol{x} \quad \text{and} \quad \overline{\mathcal{R}}_{2,b} = \frac{1}{V}\int_{\mathcal{V}} \frac{k_{f,2}}{K_{\mathrm{eq}}(T_h)} n_A n_e n_{A^+}\, d^3\boldsymbol{x}.$$

While these reaction rates depend on n_e and clearly evolve, τ_{rec} provides an estimate of the time for $\overline{n}_e V$ electrons to completely recombine at a constant rate $(\overline{\mathcal{R}}_{1,b} + \overline{\mathcal{R}}_{2,b})V$.

TABLE V. Relative change in various quantities at $t = t_{V_{\max}}$ and $r = 0$ resulting from a decrease in Δt by a factor of 4.

p_∞ [atm]	L [mm]	$\Delta t_{V_{\max}}/t_{V_{\max}}$	$\Delta T_h/T_h$	$\Delta T_e/T_e$	$\Delta X_e/X_e$
0.1	0.29	1.7×10^{-4}	4.4×10^{-5}	3.2×10^{-5}	1.1×10^{-4}
1.0	1.16	9.9×10^{-4}	9.2×10^{-6}	5.1×10^{-6}	4.6×10^{-5}
10.0	4.62	1.1×10^{-4}	1.0×10^{-6}	1.3×10^{-6}	5.8×10^{-5}

The thermal relaxation timescale τ_{rel} in Table II is based on the relaxation time in (4), with constituents $\overline{\tau}_{ek} = \tau_{ek}(\overline{n}_k, \overline{T}_e)$ for $k = A$ and A^+ set by (A11) evaluated for $\overline{T}_e$ (27) and $\overline{n}_k$ (F2). This is obviously the rate at which collisions lead to thermal equilibrium $T_e = T_h$.

[1] R. G. Meyerand and A. F. Haught, Gas Breakdown at Optical Frequencies, Phys. Rev. Lett. **11**, 401 (1963).

[2] C. G. Morgan, Laser-induced breakdown of gases, Rep. Prog. Phys. **38**, 621 (1975).

[3] S. S. Harilal, B. E. Brumfield, and M. C. Phillips, Lifecycle of laser-produced air sparks, Phys. Plasmas **22**, 063301 (2015).

[4] N. G. Glumac, G. S. Elliott, and M. Boguszko, Temporal and spatial evolution of a laser spark in air, AIAA J. **43**, 1984 (2005).

[5] M. Nishihara, J. B. Freund, and G. S. Elliott, A study of velocity, temperature, and density in the plasma generated by laser-induced breakdowns, J. Phys. D **53**, 105203 (2019).

[6] S. Brieschenk, S. O'Byrne, and H. Kleine, Visualization of jet development in laser-induced plasmas, Opt. Lett. **38**, 664 (2013).

[7] T. A. Spiglanin, A. McIlroy, E. W. Fournier, R. B. Cohen, and J. A. Syage, Time-resolved imaging of flame kernels: Laser spark ignition of $H_2/O_2/Ar$ mixtures, Combust. Flame **102**, 310 (1995).

[8] D. Bradley, C. G. W. Sheppard, I. M. Suardjaja, and R. Woolley, Fundamentals of high-energy spark ignition with lasers, Combust. Flame **138**, 55 (2004).

[9] J. M. Wang, D. A. Buchta, and J. B. Freund, Hydrodynamic ejection by laser-induced optical breakdown, J. Fluid Mech. **888**, A16-1 (2020).

[10] M. H. Morsy and S. H. Chung, Numerical simulation of front lobe formation in laser-induced spark ignition of CH_4/air mixtures, Proc. Combust. Inst. **29**, 1613 (2002).

[11] T. X. Phuoc, Laser-induced spark ignition fundamental and applications, Optics Lasers Eng. **44**, 351 (2006).

[12] L. Wermer, J. K. Lefkowitz, T. Ombrello, and S.-K. Im, Ignition enhancement by dual-pulse laser-induced spark ignition in a lean premixed methane-air flow, Proc. Combust. Inst. **37**, 5605 (2019).

[13] J. E. Retter, N. G. Glumac, and G. S. Elliott, XPACC: Stand burner ignition profiles, Technical report, Center for Exascale Simulation of Plasma-coupled Combustion, University of Illinois at Urbana-Champaign (2017).

[14] J. M. Wang and J. B. Freund, Hydrodynamic ejections by dual-pulse laser-induced breakdowns, AIAA J. **58**, 3544 (2020).

[15] H. R. Griem, Validity of local thermal equilibrium in plasma spectroscopy, Phys. Rev. **131**, 1170 (1963).

[16] D. W. Hahn and N. Omenetto, Laser-induced breakdown spectroscopy (LIBS), part I: Review of basic diagnostics and plasma–particle interactions: Still-challenging issues within the analytical plasma community, Appl. Spectrosc. **64**, 335A (2010).

[17] G. Cristoforetti, E. Tognoni, and L. A. Gizzi, Thermodynamic equilibrium states in laser-induced plasmas: From the general case to laser-induced breakdown spectroscopy plasmas, Spectrochim. Acta B **90**, 1 (2013).

[18] S. Ghosh and K. Mahesh, Numerical simulation of the fluid dynamic effects of laser energy deposition in air, J. Fluid Mech. **605**, 329 (2008).

[19] C. Dumitrache, A. Gallant, N. Minesi, S. Stepanyan, G. D. Stancu, and C. O. Laux, Hydrodynamic regimes induced by nanosecond pulsed discharges in air: Mechanism of vorticity generation, J. Phys. D **52**, 364001 (2019).

[20] R. Kandala and G. V. Candler, Numerical studies of laser-induced energy deposition for supersonic flow control, AIAA J. **42**, 2266 (2004).

[21] N. Ohnishi, M. Tate, and Y. Ogino, Computational study of shock wave control by pulse energy deposition, Shock Waves **22**, 521 (2012).

[22] A. Munafò, A. Alberti, C. Pantano, J. B. Freund, and M. Panesi, A computational model for nanosecond pulse laser-plasma interactions, J. Comput. Phys. **406**, 109190 (2019).

[23] A. Alberti, A. Munafò, M. Koll, M. Nishihara, C. Pantano, J. B. Freund, G. S. Elliott, and M. Panesi, Laser-induced non-equilibrium plasma kernel dynamics, J. Phys. D **53**, 025201 (2020).

[24] A. Alberti, A. Munafò, C. Pantano, J. B. Freund, and M. Panesi, Collinear dual-pulse laser optical breakdown and energy deposition, J. Phys. D **53**, 205202 (2020).

[25] J. P. Appleton and K. N. C. Bray, The conservation equations for a non-equilibrium plasma, J. Fluid Mech. **20**, 659 (1964).

[26] J.-H. Lee, Basic governing equations for the flight regimes of aeroassisted orbital transfer vehicles, *19th Thermophysics Conference* (AIAA, 1985).

[27] P. A. Gnoffo, R. N. Gupta, and J. L. Shinn, Conservation equations and physical models for hypersonic air flows in thermal and chemical nonequilibrium, *National Aeronautics and Space Administration, Office of Management, Scientific and Technical Information Division*, Vol. 2867 (NASA, 1989).

[28] W. G. Vincenti and C. H. Kruger, *Introduction to Physical Gas Dynamics* (John Wiley & Sons, New York, 1965).

[29] A. Mani, J. Larsson, and P. Moin, Suitability of artificial bulk viscosity for large-eddy simulation of turbulent flows with shocks, J. Comput. Phys. **228**, 7368 (2009).

[30] S. Kawai, S. K. Shankar, and S. K. Lele, Assessment of localized artificial diffusivity scheme for large-eddy simulation of compressible turbulent flows, J. Comput. Phys. **229**, 1739 (2010).

[31] R. S. Devoto, Transport properties of ionized monatomic gases, Phys. Fluids **9**, 1230 (1966).

[32] A. Fridman and L. A. Kennedy, *Plasma Physics and Engineering*, 2nd ed. (CRC Press, 2015).

[33] W. S. Liu, B. T. Whitten, and I. I. Glass, Ionizing argon boundary layers, Part 1, Quasi-steady flat-plate laminar boundary-layer flows, J. Fluid Mech. **87**, 609 (1978).

[34] R. S. Devoto, Simplified expressions for the transport properties of ionized monatomic gases, Phys. Fluids **10**, 2105 (1967).

[35] R. N. Gupta, J. M. Yos, R. A. Thompson, and K.-P. Lee, A review of reaction rates and thermodynamic and transport properties for an 11-species air model for chemical and thermal nonequilibrium calculations to 30,000 K, NASA Technical Memorandum 101528 (1990).

[36] I. I. Glass and W. S. Liu, Effects of hydrogen impurities on shock structure and stability in ionizing monatomic gases. Part 1. Argon, J. Fluid Mech. **84**, 55 (1978).

[37] M. I. Hoffert and H. Lien, Quasi-one-dimensional, nonequilibrium gas dynamics of partially ionized two-temperature argon, Phys. Fluids **10**, 1769 (1967).

[38] Y. B. Zeldovich and Y. P. Raizer, *Physics of Shock Waves and High-Temperature Hydrodynamic Phenomena*, Vol. 1 (Academic Press, 1966).

[39] J. R. Wilson, Laser-induced multiple breakdown in gases, J. Phys. D **3**, 2005 (1970).

[40] R. Adelgren, G. S. Elliot, D. Knight, A. Zheltovodov, and T. Beutner, Energy deposition in supersonic flows, in *39th Aerospace Sciences Meeting and Exhibit* (AIAA, Reno, Nevada, 2001), p. 885.

[41] N. G. Glumac and G. S. Elliott, The effect of ambient pressure on laser-induced plasmas in air, Optics Lasers Eng. **45**, 27 (2007).

[42] M. Nishihara, J. B. Freund, N. G. Glumac, and G. S. Elliott, Influence of mode-beating pulse on laser-induced plasma, J. Phys. D **51**, 135601 (2018).

[43] Ş. Yalçin, D. R. Crosley, G. P. Smith, and G. W. Faris, Influence of ambient conditions on the laser air spark, Appl. Phys. B **68**, 121 (1999).

[44] M. Capitelli, F. Capitelli, and A. Eletskii, Non-equilibrium and equilibrium problems in laser-induced plasmas, Spectrochim. Acta B **55**, 559 (2000).

[45] G. Cristoforetti, A. De Giacomo, M. Dell'Aglio, S. Legnaioli, E. Tognoni, V. Palleschi, and N. Omenetto, Local thermodynamic equilibrium in laser-induced breakdown spectroscopy: Beyond the McWhirter criterion, Spectrochim. Acta B **65**, 86 (2010).

[46] A. V. Bulgakov and N. M. Bulgakova, Dynamics of laser-induced plume expansion into an ambient gas during film deposition, J. Phys. D **28**, 1710 (1995).

[47] H. C. Le, D. E. Zeitoun, J. D. Parisse, M. Sentis, and W. Marine, Modeling of gas dynamics for a laser-generated plasma: Propagation into low-pressure gases, Phys. Rev. E **62**, 4152 (2000).

[48] S. K. Lele, Compact finite difference schemes with spectral-like resolution, J. Comput. Phys. **103**, 16 (1992).

[49] J. C. Sutherland and C. A. Kennedy, Improved boundary conditions for viscous, reacting, compressible flows, J. Comput. Phys. **191**, 502 (2003).

[50] J. B. Freund, Proposed inflow/outflow boundary condition for direct computation of aerodynamic sound, AIAA J. **35**, 740 (1997).

[51] T. Colonius, Modeling artificial boundary conditions for compressible flow, Annu. Rev. Fluid Mech. **36**, 315 (2004).

[52] T. X. Phuoc, C. M. White, and D. H. McNeill, Laser spark ignition of a jet diffusion flame, Optics Lasers Eng. **38**, 217 (2002).

[53] J. F. MacArt, J. M. Wang, P. P. Popov, and J. B. Freund, Detailed simulation of laser-induced ignition, spherical-flame acceleration, and the origins of hydrodynamic instability, in Proc. Combust. Inst. (2020).

[54] M. G. Kapper and J.-L. Cambier, Ionizing shocks in argon. Part I: Collisional-radiative model and steady-state structure, J. Appl. Phys. **109**, 113308 (2011).

[55] H. L. Brode, Numerical solutions of spherical blast waves, J. Appl. Phys. **26**, 766 (1955).

[56] M. P. Friedman, A simplified analysis of spherical and cylindrical blast waves, J. Fluid Mech. **11**, 1 (1961).

[57] L. J. Radziemski and D. A. Cremers, *Lasers-Induced Plasmas and Applications* (Marcel Dekker, New York, NY, 1989).

[58] T. X. Phuoc and F. P. White, Laser-induced spark ignition of CH_4/air mixtures, Combust. Flame **119**, 203 (1999).

[59] Y. Ling and S. Balachandar, Asymptotic scaling laws and semi-similarity solutions for a finite-source spherical blast wave, J. Fluid Mech. **850**, 674 (2018).

[60] A. Kramida, Y. Ralchenko, and J. Reader, NIST Atomic Spectra Database (version 5.7.1), National Institute of Standards and Technology, Gaithersburg MD, https://doi.org/10.18434/T4W30F.

[61] R. J. Kee, M. E. Coltrin, and P. Glarborg, *Chemically Reacting Flow: Theory and Practice* (John Wiley & Sons, 2005).

[62] R. S. Devoto, Transport coefficients of ionized argon, Phys. Fluids **16**, 616 (1973).

[63] Y. Enomoto, Wall boundary layer effects on ionizing shock structure in argon, J. Phys. Soc. Jpn. **35**, 1228 (1973).

[64] J. M. Yos, Transport properties of nitrogen, hydrogen, oxygen, and air to 30,000 K, Technical Memorandum RAD-TM-63-7, Research and Advanced Development Division, AVCO Corporation, Wilmington, MA (1963).

[65] L. Spitzer, Jr. and R. Härm, Transport phenomena in a completely ionized gas, Phys. Rev. **89**, 977 (1953).

[66] M. G. Kapper and J.-L. Cambier, Ionizing shocks in argon. Part II: Transient and multi-dimensional effects, J. Appl. Phys. **109**, 113309 (2011).

[67] P. E. Oettinger and D. Bershader, A unified treatment of the relaxation phenomenon in radiating argon plasma flows, AIAA J. **5**, 1625 (1967).

[68] D. Meiners and C. O. Weiss, Continuous emission of argon, krypton and xenon plasmas, J. Quant. Spectrosc. Radiat. Transfer **16**, 273 (1976).

[69] K. P. Horn, H. Wong, and D. Bershader, Radiative behaviour of a shock-heated argon plasma flow, J. Plasma Phys. **1**, 157 (1967).

[70] A. Munafò, N. N. Mansour, and M. Panesi, A reduced-order NLTE kinetic model for radiating plasmas of outer envelopes of stellar atmospheres, Astrophys. J. **838**, 126 (2017).

[71] W. L. Wiese, J. W. Brault, K. Danzmann, V. Helbig, and M. Kock, Unified set of atomic transition probabilities for neutral argon, Phys. Rev. A **39**, 2461 (1989).

[72] D. V. Gaitonde and M. R. Visbal, Pade-type higher-order boundary filters for the Navier–Stokes equations, AIAA J. **38**, 2103 (2000).

[73] J. Haidar, Non-equilibrium modelling of transferred arcs, J. Phys. D **32**, 263 (1999).

[74] J. P. Trelles, J. V. R. Heberlein, and E. Pfender, Non-equilibrium modelling of arc plasma torches, J. Phys. D **40**, 5937 (2007).

[75] J. Crank, *The Mathematics of Diffusion*, 2nd ed. (Oxford University Press, 1975).